

NNLO non-resonant corrections to threshold top-pair production from e^+e^- collisions: Endpoint-singular terms

B. JANTZEN^a and P. RUIZ-FEMENÍA^b

^a*Institut für Theoretische Teilchenphysik und Kosmologie,
RWTH Aachen University,
D-52056 Aachen, Germany*

^b*Instituto de Física Corpuscular (IFIC), CSIC-Universitat de València
Apartado de Correos 22085, E-46071 Valencia, Spain*

Abstract

We analyse the subleading non-resonant contributions to the $e^+e^- \rightarrow W^+W^-b\bar{b}$ cross section at energies near the top-antitop threshold. These correspond to next-to-next-to-leading-order (NNLO) corrections with respect to the leading-order resonant result. We show that these corrections produce $1/\epsilon$ endpoint singularities which precisely cancel the finite-width divergences arising in the resonant production of the $W^+W^-b\bar{b}$ final state from on-shell decays of the top and anti-top quarks at the same order. We also provide analytic results for the $(m_t/\Lambda)^2$, (m_t/Λ) and $(m_t/\Lambda)^0 \log \Lambda$ terms that dominate the expansion in powers of (Λ/m_t) of the complete set of NNLO non-resonant corrections, where Λ is a cut imposed on the invariant masses of the bW pairs that is neither too tight nor too loose ($m_t\Gamma_t \ll \Lambda^2 \ll m_t^2$).

1 Introduction

An e^+e^- linear collider (LC) is probably the most compelling case as the next-generation particle collider for high-precision physics. One of the LC options, the International Linear Collider, has recently completed its technical design, and there is hope that funding to begin its construction could be gathered up in a near future, especially if Japan's proposal to host it goes forward. The physics motivation for a linear collider has been strengthened even more after the discovery of a new particle compatible with a Higgs boson at the LHC whose interactions could be studied at the LC with sufficient precision to test the Electroweak Symmetry Breaking (EWSB) mechanism of the Standard Model. The LC would also probe the dynamics behind the symmetry breaking mechanism through high-precision measurements of the properties of the top quark, the heaviest of the fundamental fermions and thus the most strongly coupled to the EWSB sector. The flexibility in energy of a LC would allow the top–antitop threshold behaviour to be mapped out in detail. Particularly, a theoretically well-defined top mass with a total uncertainty below 100 MeV could be extracted by means of such a threshold scan [1, 2], substantially beyond the precision achieved at Tevatron, $m_t = 173.18 \pm 0.56(\text{stat}) \pm 0.75(\text{syst})$ GeV [3], and at the LHC at 7 TeV, $m_t = 173.3 \pm 0.5(\text{stat}) \pm 1.3(\text{syst})$ GeV [4]. While the statistical uncertainty of the top mass measurement at the LHC is expected to improve in future runs, the systematic (theoretical) uncertainties related to the connection between the mass parameter used in the theory and the one measured in the experiment are a limiting factor for further improving the accuracy of the top-quark mass measurement at hadron colliders.

The perturbative nature of the $t\bar{t}$ system which is produced near threshold in e^+e^- annihilation was recognized long ago [5], and the leading-order Coulomb force was treated to all orders in α_s using a non-relativistic approach [6–8]. The matching between QCD and non-relativistic QCD (NRQCD) [9] provided the necessary pieces to compute the next-to-next-to-leading order (NNLO) QCD corrections to the $t\bar{t}$ production cross section [10] in the region defined by relative velocities of the top and antitop $v \sim \alpha_s$. In this fixed-order approach which achieves a systematic summation of terms $\alpha_s^n v^{m+1}$ with $n + m \leq k$ at order $N^k\text{LO}$, up to $N^3\text{LO}$ corrections to resonant $t\bar{t}$ production are known [11–13]. In parallel, the advances in the formulation of the non-relativistic effective theory allowed for renormalization-group improved calculations for the $t\bar{t}$ system produced at threshold. Within the potential NRQCD (pNRQCD) [14–17] and velocity NRQCD (vNRQCD) [18–20] formalisms the systematic summation of potentially large logarithmic terms $(\alpha_s \log v)^n$ originating from ratios of the top-mass scale m_t , the non-relativistic three-momentum $\vec{p} \sim m_t v$ and the kinetic energy $E \sim m_t v^2$, was carried out to next-to-next-to-leading logarithmic (NNLL) order [21–24] for the total cross section, which accounts for all terms proportional to $\alpha_s^n v^{m+1} \log^\ell v$ with $n + m - \ell \leq 2$.

The effective field theory (EFT) computations above account for the QCD interactions among nearly on-shell top and antitop quarks. However, the predictions can only be evaluated for all threshold energies after the top decay width is included in the EFT quark propagator, $(E - \vec{p}^2/2m_t + i\Gamma_t)^{-1}$, thus providing an infrared cutoff for the top

kinetic energy. The counting $\Gamma_t \sim m_t v^2 \sim m_t \alpha_s^2$ is naturally enforced in this way, which is also justified numerically in the Standard Model, where $\Gamma_t \approx 1.5$ GeV due to the electroweak interaction. Once the top width is included, the physical final state is $W^+W^-b\bar{b}$ – at least if we assume that $V_{tb} \approx 1$, and consider W bosons as stable. Beyond leading order, the production of the final state $W^+W^-b\bar{b}$ can also occur through non-resonant processes that do not involve a nearly on-shell $t\bar{t}$ pair, and which are thus not described by the standard NRQCD formalism. In the counting scheme where the electroweak coupling scales as $\alpha_{\text{EW}} \sim \alpha_s^2$, the leading non-resonant effects are NLO for the total cross section and reproduce the full-theory contributions where one of the bW pairs is produced from a nearly on-shell top, while the other is produced either from a highly virtual top or directly without an intermediate top. The unstable-particle EFT [25–27] provides the framework for a systematic computation of resonant and non-resonant contributions while maintaining an expansion in the small parameters of the problem. The NLO non-resonant corrections, calculated within this formalism in [28], represent the leading electroweak correction to the $t\bar{t}$ cross section below the threshold, where the LO (resonant) result rapidly vanishes, reaching up to 20%. This had been noticed before in Refs. [29, 30], obtaining the dominant NLO non-resonant corrections when moderate invariant-mass cuts on the bW pairs are applied within the so-called *phase-space matching* approach, based on vNRQCD.

Aside from the sizeable corrections induced by the non-resonant production, there is a further conceptual reason to term the pure QCD resonant result alone that is usually shown in the literature as incomplete. The resonant cross section at NNLO shows *finite-width divergences*, *i.e.* uncanceled divergences proportional to the top width, which in dimensional regularization have the form

$$\delta\sigma_{\text{res}}^{\text{NNLO}} \propto \frac{\alpha_s \Gamma_t}{\epsilon} \propto \frac{\alpha_s \alpha_{\text{EW}}}{\epsilon}, \quad (1)$$

and arise from the logarithmic divergences in the imaginary part of the two-loop non-relativistic correlation function. These are also known as *phase-space divergences* because they can be traced back to UV-divergences in the NRQCD $t\bar{t}$ phase space integrations [31] that originate because the unstable-particle propagators describing the top quark in the EFT allow for contributions to the forward-scattering amplitude from intermediate top and antitop states which have arbitrarily large invariant masses (see [32] for a detailed explanation). The occurrence of finite-width divergences is an evidence that the pure resonant result must be supplemented with additional short-distance information from the full $e^+e^- \rightarrow W^+W^-b\bar{b}$ process. In the unstable-particle EFT the additional input is given by diagrams corresponding to off-shell top quark decay that contribute to the non-resonant part at NNLO [13]. In this paper we show that the NNLO non-resonant contributions generate infrared divergences when the momentum of the virtual top-quark lines approaches the endpoint at $p_t^2 = m_t^2$, which precisely cancel the finite-width divergences (1) from the resonant part. This is proved by explicit computation of the NNLO non-resonant contributions, given by the $\mathcal{O}(\alpha_s)$ corrections to the NLO non-resonant diagrams. For the extraction of the endpoint-singular terms we use the method of regions to asymptotically expand the loop and phase-space integrals around the endpoint.

As a byproduct, we obtain the first terms in the expansion in Λ/m_t of the NNLO non-resonant contributions, where Λ is a cut on the invariant masses of the top and antitop decay products satisfying $m_t\Gamma_t \ll \Lambda^2 \ll m_t^2$. This approximation provides an accurate estimate of the NNLO non-resonant contributions to the $t\bar{t}$ inclusive cross section with moderate invariant-mass cuts in the bW systems, and, as we prove, confirms the result obtained for the same observable within the phase-space matching approach in [30].

The structure of the paper is the following. In Section 2 we recall the issue of the uncanceled divergences proportional to the top width in resonant $t\bar{t}$ production at NNLO and collect the total divergent result. The framework to account for non-resonant production at NLO and NNLO is described in Section 3. The origin of the endpoint singularities that arise in the non-resonant amplitudes and the method used for their analytic extraction is explained in the latter Section, which includes the introduction of the scale Λ . The results for the endpoint-singular contributions to the NNLO non-resonant corrections are summarized in Section 4 for the various sets of diagrams. Readers not interested in the individual results might jump directly to Section 4.4, where the formula containing all endpoint-singular non-resonant NNLO contributions to the $e^+e^- \rightarrow W^+W^-b\bar{b}$ cross section with an invariant-mass cut Λ is given and the cancellation of the finite-width divergences against the endpoint divergences is made explicit. In Section 5 we compare our findings with those of the phase-space matching approach [30] and also comment on the approximation to the NNLO non-resonant contributions obtained in another work [33] by expanding in $\rho = 1 - M_W/m_t$. Finally, in Section 6 we compare the non-resonant contributions computed in this work with the NLO ones as a function of the cut Λ , and then show their numerical impact as a function of the energy relative to the leading-order QCD calculation of resonant $t\bar{t}$ production. Our conclusions are given in Section 7.

2 NNLO resonant contributions: Finite-width divergences

Close to the top-antitop production threshold, the $W^+W^-b\bar{b}$ final state is produced from e^+e^- collisions predominantly by intermediate top and antitop quarks with small virtuality (resonant), *i.e.* $p_t^2 - m_t^2 \sim m_t^2 v^2$, where $v^2 = (E + i\Gamma_t)/m_t$ and $E = \sqrt{s} - 2m_t$ is the non-relativistic kinetic energy. The QCD dynamics of the nearly on-shell top and antitop quarks can be described within the NRQCD approach, an effective field theory that is built upon integrating out the hard modes with scale $\sim m_t$. Since the inclusive cross section for the $e^+e^- \rightarrow W^+W^-b\bar{b}$ process can be obtained from the $W^+W^-b\bar{b}$ cuts of the e^+e^- forward-scattering amplitude, the resonant contribution to this observable is given in the EFT formalism by the imaginary part of the matrix element

$$i\mathcal{A}_{\text{res}} = \sum_{k,l} C_p^{(k)} C_p^{(l)} \int d^4x \langle e^- e^+ | T[i\mathcal{O}_p^{(k)\dagger}(0) i\mathcal{O}_p^{(l)}(x)] | e^- e^+ \rangle, \quad (2)$$

where $\mathcal{O}_p^{(l)}(x)$ ($\mathcal{O}_p^{(k)\dagger}(x)$) are operators describing the production (decay) of the resonant $t\bar{t}$ pair from e^+e^- , and $C_p^{(k,l)}$ are short-distance coefficients. At leading order in the

non-relativistic expansion, the $t\bar{t}$ pair is produced in an S -wave, and the first term in (2) is of order $\alpha_{\text{EW}}^2 v$. The corresponding LO production operators can be found in [28]. At NNLO, P -wave production operators, as well as new (v^2 -suppressed) S -wave operators contribute (for explicit expressions see [30]). The perturbative contributions to the resonant amplitude (2) are characterized by top and antitop quark lines with time and spatial components of the momenta obeying the potential scaling, $p_t^0 - m_t \sim m_t v^2$ and $\vec{p}_t \sim m_t v$ (in the centre-of-mass system or in a reference frame differing from it only by a small non-relativistic velocity).

As mentioned in the introduction, at NNLO the resonant amplitude (2) shows an uncanceled finite-width divergence in the imaginary part. The finite-width divergences arise from two-loop diagrams with a Coulomb gluon and a v^2 -suppressed insertion. The insertion may correspond to a v^2 -suppressed potential, an NNLO correction to the kinetic Lagrangian, a P -wave or a v^2 -suppressed S -wave current producing the top–antitop pair, or an insertion of the absorptive part of matching coefficients of production operators describing finite lifetime corrections. The different contributions to the NNLO finite-width divergence are collected in the following formula:

$$\begin{aligned} \text{div } \sigma_{\text{res}}^{\text{NNLO}} = & \left[(C_p^{(v)})^2 + (C_p^{(a)})^2 \right] 2 N_c \left(-4\pi a \text{div} [\text{Im } G_r] + \text{div} [\text{Im } G_{\text{kin}}] \right. \\ & \left. + \text{div} [\text{Im } G_{\text{dil}}] + \text{div} [\text{Im } G_{v^2}] \right) \\ & + \left[(C_{p,P\text{-wave}}^{(v)})^2 + (C_{p,P\text{-wave}}^{(a)})^2 \right] \frac{4N_c}{3m_t^2} \text{div} [\text{Im } G_{P\text{-wave}}] \\ & + [C_p^{(v)} C_p^{(v),\text{abs}} + C_p^{(a)} C_p^{(a),\text{abs}}] 4N_c \text{div} [\text{Re } G_C^{(0)}], \end{aligned} \quad (3)$$

where

$$C_p^{(v)} = 4\pi\alpha \left[\frac{Q_t Q_e}{s} + \frac{v_e v_t}{s - M_Z^2} \right], \quad C_p^{(a)} = -4\pi\alpha \frac{a_e v_t}{s - M_Z^2}, \quad (4)$$

$$C_{p,P\text{-wave}}^{(v)} = 4\pi\alpha \frac{v_e a_t}{s - M_Z^2}, \quad C_{p,P\text{-wave}}^{(a)} = -4\pi\alpha \frac{a_e a_t}{s - M_Z^2} \quad (5)$$

are the tree-level coefficient functions of the leading-order S - and P -wave production operators, and $a \equiv C_F \alpha_s$, with $C_F = 4/3$ the Casimir operator of the fundamental SU(3) representation. The vector (v_f) and axial-vector (a_f) couplings of the fermions to the gauge bosons are given in Eq. (27) below, and the remaining symbols are defined as in [28]. The $C_p^{(v/a),\text{abs}}$ are the absorptive parts of the matching coefficients of the leading-order S -wave production operators. The latter contributions are part of the corrections induced by the top-quark instability, as they can be interpreted as top-pair production where one of the tops arises from a bW system with invariant mass very close to m_t^2 . The coefficients $C_p^{(v),\text{abs}}$ and $C_p^{(a),\text{abs}}$ were calculated in Ref. [31] (there denoted $C_V^{bW,\text{abs}}$ and $C_A^{bW,\text{abs}}$, respectively), and their explicit expressions can be found therein. They

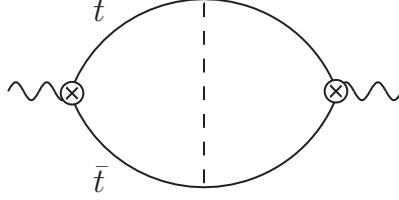


Figure 1: Two-loop resonant NRQCD graph with a Coulomb potential.

are suppressed by $\alpha_{\text{EW}} \sim \Gamma_t/m_t$ with respect to the leading-order $C_p^{(v/a)}$, and therefore amount to NNLO corrections. The absorptive parts in the matching coefficients of the $t\bar{t}$ production currents lead to a dependence of the cross section on the real part of the zero-distance Coulomb Green function $G_C^{(0)}$, which has a divergence from the two-loop graph with a Coulomb potential shown in Fig. 1,

$$\text{div}[\text{Re } G_C^{(0)}] = \frac{m_t^2 a}{16\pi} \frac{1}{\epsilon}, \quad (6)$$

here regulated dimensionally.

The remaining contributions to $\text{div } \sigma_{\text{res}}^{\text{NNLO}}$ in (3) arise from divergent contributions to the imaginary part of the Green function: G_r , G_{kin} and G_{dil} are first-order corrections to the zero-distance Green function from the potential $\tilde{V}_r(\vec{p}, \vec{q}) = (\vec{p}^2 + \vec{q}^2)/2m_t^2(\vec{p} - \vec{q})^2$ (in momentum space, leaving out the corresponding Wilson coefficient), the insertion of the kinetic energy correction $\vec{\partial}^4/(8m_t^3)$, and the insertion of the lifetime-dilatation operator $i\Gamma_t \vec{\partial}^2/(4m_t^2)$, respectively. The explicit expressions for G_r , G_{kin} and G_{dil} in $d = 4 - 2\epsilon$ dimensions can be found in Ref. [31]. Their divergent parts satisfy

$$\text{div}[\text{Im } G_{\text{kin}}] = -\text{div}[\text{Im } G_{\text{dil}}] = -(4\pi a) \text{div}[\text{Im } G_r] = \frac{m_t a}{16\pi} \frac{\Gamma_t}{\epsilon}. \quad (7)$$

The term G_{v^2} corresponds to the zero-distance Coulomb Green function obtained with the top–antitop pair produced by the v^2 -suppressed S -wave current, which can easily be related to the leading-order Coulomb Green function by the non-relativistic equation of motion of the top quark, $G_{v^2} = -(v^2/3)G_C^{(0)}$. Therefore,

$$\text{div}[\text{Im } G_{v^2}] = -\frac{\Gamma_t}{3m_t} \text{div}[\text{Re } G_C^{(0)}] = -\frac{m_t a}{48\pi} \frac{\Gamma_t}{\epsilon}. \quad (8)$$

Finally, $G_{P\text{-wave}}$ is the $\ell = 1$ component of the Coulomb Green function at zero distance and describes the production of the top–antitop pair in a P -wave, which first contributes at NNLO. From the explicit expression of $G_{P\text{-wave}}$ (see *e.g.* Ref. [31], denoted G^1 therein) we have

$$\text{div}[\text{Im } G_{P\text{-wave}}] = \frac{m_t^3 a}{16\pi} \frac{\Gamma_t}{\epsilon}. \quad (9)$$

Using the results (6)–(9) in (3), we get the total finite-width divergence at NNLO:

$$\begin{aligned} \text{div } \sigma_{\text{res}}^{\text{NNLO}} = \frac{C_F N_c \alpha_s m_t \Gamma_t}{12\pi \epsilon} & \left[(C_p^{(v)})^2 + (C_p^{(a)})^2 + (C_{p,P\text{-wave}}^{(v)})^2 + (C_{p,P\text{-wave}}^{(a)})^2 \right. \\ & \left. + \frac{3m_t}{\Gamma_t} (C_p^{(v)} C_p^{(v),\text{abs}} + C_p^{(a)} C_p^{(a),\text{abs}}) \right]. \end{aligned} \quad (10)$$

The result in (10) agrees with the total UV divergence generated in the NNLO effective-theory matrix elements contributing to $\sigma_{\text{res}}^{\text{NNLO}}$ as obtained in [31]. We note that in the approach followed in Refs. [30, 31], the finite-width divergences (named phase-space divergences therein) are absorbed by the counterterms $\delta\tilde{C}_{V/A}$ associated to $(e^+e^-)(e^+e^-)$ forward-scattering operators, and the corresponding phase-space logarithms are resummed using renormalization-group techniques known from effective theories for the coefficients $\tilde{C}_{V/A}$. The matching conditions for these coefficients at the hard scale, $\tilde{C}_{V/A}(\nu = 1)$, are related to the non-resonant contributions in the unstable-particle effective theory approach which we discuss in the following section.

3 Endpoint divergences in the non-resonant contributions

The non-relativistic EFT formalism has to be extended in order to account for non-resonant production of the physical final state $W^+W^-b\bar{b}$, which involves processes where the bW pairs are produced by highly virtual top or antitop quarks, $p_t^2 - m_t^2 \sim \mathcal{O}(m_t^2)$, or without intermediate tops. The leading non-resonant contributions are caused by the top-quark instability, and are thus of electroweak origin. Adopting the counting scheme where $\alpha_{\text{EW}} \sim \alpha_s^2$, a systematic separation of resonant and non-resonant effects can be achieved within the unstable-particle effective theory for pair production near threshold [25–27, 31]. Non-resonant effects take place at short distances, as compared to the length scales governing the QCD interaction of the non-relativistic top–antitop pair. The non-resonant contributions to the e^+e^- forward-scattering amplitude are thus reproduced in this formalism by the matrix element of four-electron production–decay operators $\mathcal{O}_{4e}^{(k)}(0)$ [25, 26, 31]:

$$i\mathcal{A}_{\text{non-res}} = \sum_k C_{4e}^{(k)} \langle e^- e^+ | i\mathcal{O}_{4e}^{(k)}(0) | e^- e^+ \rangle, \quad (11)$$

with short-distance coefficients $C_{4e}^{(k)}$ that are determined by the hard contributions of the e^+e^- forward-scattering amplitude. Explicit expressions for the operators $\mathcal{O}_{4e}^{(k)}$ can be found in [28].

For the $W^+W^-b\bar{b}$ inclusive cross section, only the imaginary parts of $C_{4e}^{(k)}$ are needed. The first non-vanishing contribution arises from the cut two-loop diagrams of order α_{EW}^3 shown in Fig. 2, and is thus suppressed by $\alpha_{\text{EW}}/v \sim v$ (NLO) with respect to the leading

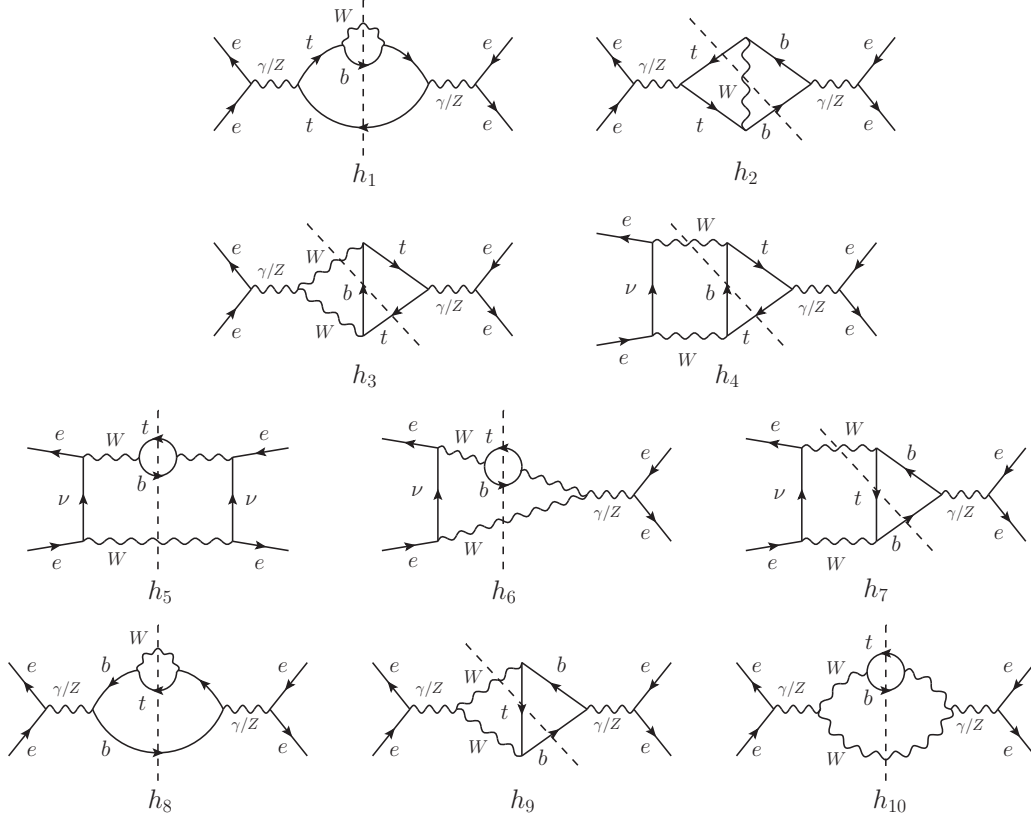


Figure 2: Two-loop forward-scattering amplitude diagrams with $bW^+\bar{t}$ cuts contributing to the NLO non-resonant cross section. $\bar{b}W^-t$ cuts and symmetric diagrams are not shown. This figure is reproduced from Ref. [28].

term from the resonant part.¹ The diagrams in Fig. 2 are obtained by asymptotically expanding the full electroweak theory diagrams of the e^+e^- forward-scattering amplitude assuming that the momenta in the top and antitop lines are hard, so that the top quarks are far off-shell, $p_t^2 - m_t^2 \sim \mathcal{O}(m_t^2)$. This expansion implies that the top-quark self-energy insertions (resummed in the full-theory diagrams in the top-quark propagator), $m_t \Sigma(p_t^2) \sim m_t^2 \alpha_{\text{EW}} \ll p_t^2 - m_t^2$, must be treated perturbatively. Accordingly, top-quark propagators in the non-resonant diagrams have no width, contrary to the case of resonant top quarks. The leading-order imaginary contribution in this non-resonant expansion of the top propagator is proportional to $\delta(p_t^2 - m_t^2)$, yielding the 3-particle final states $bW^+\bar{t}$ (Fig. 2) and $\bar{b}W^-t$ instead of the physical 4-particle final state $W^+W^-b\bar{b}$. In addition,

¹We do not consider other $\mathcal{O}(\alpha_{\text{EW}}^3)$ contributions where the $b\bar{b}$ or the W^+W^- pair in the final state is reached through the resonant decay of a Higgs or Z -boson, since the latter constitute a reducible background which can be eliminated in the $t\bar{t}$ resonance region by applying cuts on the invariant masses of the final-state particle pairs [28].

the amplitudes corresponding to the diagrams in Fig. 2 have to be expanded in v in the threshold region. Altogether, the non-resonant contribution at NLO amounts to the calculation of the squared and phase-space integrated amplitudes for the on-shell processes $e^+e^- \rightarrow \bar{b}W^-t$ and $e^+e^- \rightarrow bW^+\bar{t}$ at the centre-of-mass energy $s = 4m_t^2$ in ordinary perturbation theory (see [28]). The NLO non-resonant corrections to the $W^+W^-b\bar{b}$ cross section, also including cuts on the invariant masses of the bW systems, were determined in [28] and later confirmed by [33].

Divergences in the non-resonant part can arise when the top (or antitop) propagators go on-shell [28, 32]. This is a consequence of the hard-momentum region expansion, which forces us to drop the top width from the top–antitop propagators. Given that dimensional regularization is used to deal with divergences in the resonant amplitude, it must also be used here consistently in order to regulate phase-space singularities from top-quark propagators going on-shell. For the 3-particle $bW^+\bar{t}$ phase space, the outer integration variable can be chosen as the squared invariant mass of the bW^+ subsystem, p_t^2 , where $p_t = p_b + p_W$. The antitop momentum is on-shell here, $p_{\bar{t}}^2 = m_t^2$. Setting $s = 4m_t^2$, as dictated by the asymptotic expansion, the kinematics of the process provides the restriction $m_t^2 - \Lambda^2 \leq p_t^2 \leq m_t^2$, where $\Lambda^2 = 2m_t\Delta M_t - \Delta M_t^2$ is introduced to allow for loose cuts ($\Lambda^2 \gg m_t\Gamma_t$ or $\Delta M_t \gg \Gamma_t$) in the bW invariant masses of the form [28]

$$m_t - \Delta M_t \leq \sqrt{p_{t,\bar{t}}^2} \leq m_t + \Delta M_t. \quad (12)$$

For the $\bar{b}W^-t$ phase space, the roles of p_t^2 and $p_{\bar{t}}^2$ are reversed.

To recover the total cross section we have to set $\Lambda^2 = m_t^2 - M_W^2$. Integrating over all other kinematic variables but p_t^2 , each non-resonant contribution involves an integral of the form

$$\int_{m_t^2 - \Lambda^2}^{m_t^2} \frac{dp_t^2}{(m_t^2 - p_t^2)^{r+n\epsilon}} = \frac{1}{1 - r - n\epsilon} (\Lambda^2)^{1-r-n\epsilon}, \quad (13)$$

where the endpoint singularity at $p_t^2 = m_t^2$ for $r \geq 1$ has been regularized in $d = 4 - 2\epsilon$ dimensions, which drops the scaleless singular contribution from the upper boundary $p_t^2 = m_t^2$. The integrals (13) arise from expanding the non-singular parts of the numerator of the contributions about the endpoint $p_t^2 = m_t^2$. At NLO, only the diagram h_1 has an endpoint divergence, with $r = 3/2$, and the dimensionally regularized result is therefore finite in the limit $\epsilon \rightarrow 0$. At NNLO, however, integrands with $r = 1$ are found which generate $1/\epsilon$ terms of the form (1). These shall cancel the finite-width divergences in the resonant part of the full-theory diagrams.

From the unstable-particle EFT power-counting $\alpha_s \sim \alpha_{\text{EW}}^{1/2}$, NNLO non-resonant corrections can only arise from QCD corrections to the NLO ones. More precisely, the non-resonant NNLO corrections are obtained from the NLO contributions by adding to the diagrams h_1 – h_{10} in Fig. 2 a virtual gluon or QCD counterterm (on one side of the cut) or a real gluon (going through the cut) in all possible ways. The number of diagrams contributing in this way is well above 100. Fortunately, only a few of them are endpoint-singular, as we show next, first for the virtual contributions and afterwards for the real-gluon radiation diagrams.

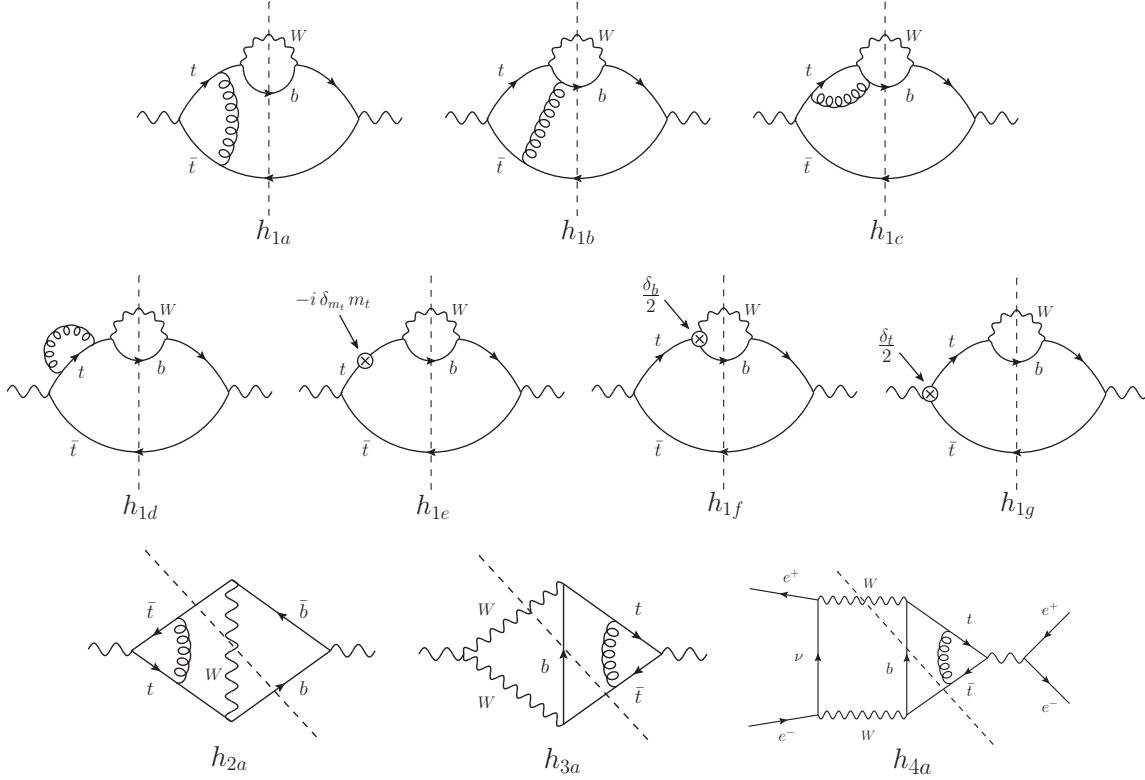


Figure 3: $\mathcal{O}(\alpha_s)$ virtual corrections to the two-loop forward-scattering diagrams with $bW^+\bar{t}$ cuts which are endpoint-singular. $\bar{b}W^-t$ cuts and symmetric diagrams are not shown. The e^+e^- external legs have not been drawn, except for the h_{4a} diagram.

NNLO amplitudes with virtual gluons (see Fig. 3) involve the same 3-particle cuts ($bW^+\bar{t}$ or $\bar{b}W^-t$) as the NLO diagrams. In order to isolate the endpoint-singular contributions, the integrand of the p_t^2 -integration in the 3-particle phase space is asymptotically expanded in powers of $(1-t)$, where $t = p_t^2/m_t^2$. A factor $(1-t)^{1/2-\epsilon}$ is provided by the kinematics of the phase space and originates from splitting the total momentum q into p_t and the on-shell antitop momentum $p_{\bar{t}}$. Negative integer powers of $(1-t)$ are introduced by top propagators. This simple counting provides the leading term $(1-t)^{-3/2-\epsilon}$ in the limit $t \rightarrow 1$ for the integrand of the NLO diagram h_1 , while diagrams h_2-h_4 , with one intermediate top propagator less, get an additional power of $(1-t)$ and are endpoint-regular. Likewise, the integrands for diagrams h_5-h_{10} , with no internal top line, exhibit the overall scaling $(1-t)^{1/2-\epsilon}$ and are well-behaved at the endpoint.

Gluon insertions can give rise to an additional power $(1-t)^{r'}$, where only $r' \leq 1/2$ is relevant for an endpoint-singular behaviour, and we note that half-integer values of r' are needed in order to produce $1/\epsilon$ endpoint divergences. The overall power in $(1-t)$ of the loop integrals involved in the virtual corrections can easily be inferred by using the expansion by regions [34–36], as it is explained in Sec. 3.1 below. Negative powers

of $(1-t)$ can arise from 1-loop integrals which (after integration over all phase-space variables but t) are singular when t approaches its maximum. This is only achieved by the gluon correction to the $t\bar{t}$ -vertex and by the virtual gluon connecting the antitop with the on-shell bottom quark radiated from a top line. The former yields negative powers with $r' = -1/2 - \epsilon$ and thus produces endpoint-singular contributions when it corrects diagrams $h_1 - h_4$ (NNLO diagrams h_{ia} , $i = 1, \dots, 4$ of Fig. 3). In particular, the negative half-integer power introduced by the $t\bar{t}$ -vertex correction in the NNLO diagrams $h_{1a} - h_{4a}$ gives integrands scaling as $(1-t)^{-2-2\epsilon}$ (for h_{1a}) and $(1-t)^{-1-2\epsilon}$ (for h_{ia} , $i = 1, \dots, 4$), where the latter produce $1/\epsilon$ endpoint divergences according to (13). On the other hand, the virtual gluon connecting the antitop with the on-shell bottom quark radiated from a top line yields factors $(1-t)^{-1-2\epsilon}$ and $(1-t)^{-1/2-\epsilon}$. However, this loop integral replaces one top propagator of the corresponding NLO diagram, so the additional powers are $r' = -2\epsilon$ and $r' = 1/2 - \epsilon$. Thus this loop integral is only of relevance when inserted into diagram h_1 (NNLO diagram h_{1b} of Fig. 3), yielding singular integrand terms scaling as $(1-t)^{-3/2-3\epsilon}$ and $(1-t)^{-1-2\epsilon}$, respectively.

The remaining virtual α_s -corrections to diagram h_1 , namely the top-bottom vertex corrections (in diagram h_{1c}), the top self-energy plus the mass counterterm (h_{1d} plus h_{1e}), as well as the tb - and $t\bar{t}$ -vertex counterterms (h_{1f} and h_{1g}), yield factors $(1-t)^{0+n\epsilon}$ at leading order and $(1-t)^{1+n\epsilon}$ at next-to-leading order, such that the corresponding diagrams have the same degree of divergence at the endpoint as the NLO diagram h_1 , and subleading terms are endpoint-regular. The same applies to the remaining virtual corrections to diagrams h_i , $i = 2, \dots, 10$, which are not shown in Fig. 3. In summary, the potentially endpoint-singular cases that can be found from a virtual gluon at NNLO are ($y \equiv 1 - \Lambda^2/m_t^2$):

$$\int_y^1 dt (1-t)^{-2-2\epsilon} \propto \frac{m_t^2}{\Lambda^2} \left(\frac{m_t^2}{\Lambda^2} \right)^{2\epsilon}, \quad \text{diagram } h_{1a}, \quad (14)$$

$$\int_y^1 dt (1-t)^{-3/2-n\epsilon} \propto \frac{m_t}{\Lambda} \left(\frac{m_t^2}{\Lambda^2} \right)^{n\epsilon}, \quad \text{diagrams } h_{1X}, X = a, \dots, g, \quad (15)$$

$$\int_y^1 dt (1-t)^{-1-n\epsilon} \propto \frac{1}{\epsilon} \left(\frac{m_t^2}{\Lambda^2} \right)^{n\epsilon} \simeq \frac{1}{\epsilon_{\text{ep}}} + n \ln \frac{m_t^2}{\Lambda^2}, \quad \text{diagrams } h_{ia}, i = 1, \dots, 4, h_{1b}. \quad (16)$$

Only in the last case (16) we obtain a $1/\epsilon$ singularity, which is labeled $1/\epsilon_{\text{ep}}$ in order to mark it as an endpoint divergence. The cases (14) and (15) are also endpoint-divergent, but finite (in the limit $\epsilon \rightarrow 0$) through dimensional regularization. The asymptotic expansion of the phase-space integral near the endpoint translates into an expansion in powers of Λ/m_t in the results. Virtual corrections to diagrams $h_5 - h_{10}$ are all endpoint-regular and contribute first at $\mathcal{O}((\Lambda/m_t)^3)$ in this expansion.

Let us turn to the NNLO non-resonant contributions with real-gluon emission which involve a 4-particle cut, $bW^+\bar{t}g$ (see Fig. 4) or $\bar{b}W^-tg$. The corresponding phase space can be written with an additional integration over the variable $t^* = p_{t^*}^2/m_t^2$ with $p_{t^*} =$

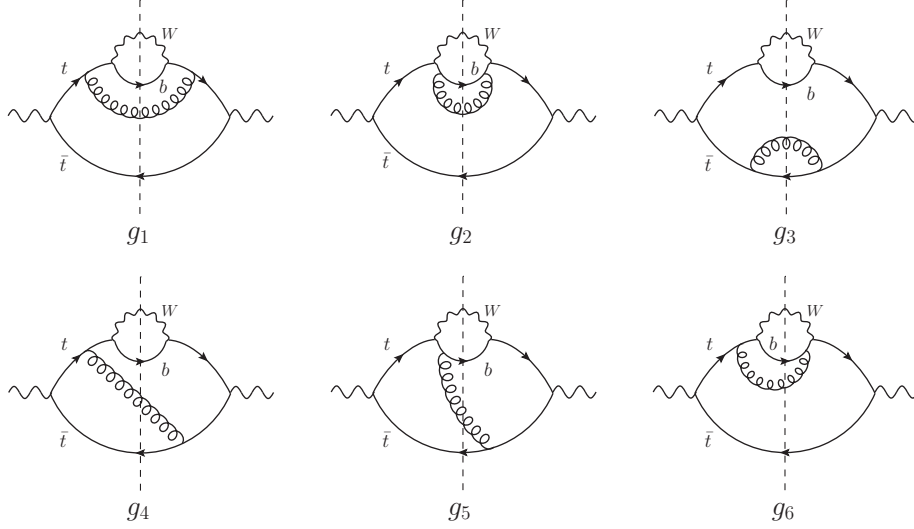


Figure 4: $\mathcal{O}(\alpha_s)$ real-gluon corrections to the two-loop forward-scattering diagrams with $bW^+\bar{t}g$ cuts which are endpoint-singular. $\bar{b}W^-tg$ cuts and symmetric diagrams are not shown. The e^+e^- external states have been omitted.

$p_b + p_W + p_g$, where p_g is the gluon momentum. The kinematic restriction for the total cross section reads $x \leq t \leq t^* \leq 1$, where $x = M_W^2/m_t^2$. Now we want to impose an invariant-mass cut in accordance with the one for the 3-particle phase space described above. An infrared-safe definition requires that the case where no gluon is emitted and the case where the bottom quark emits a collinear gluon should be indistinguishable. Note that when the bottom quark emits a collinear gluon, splitting its momentum into $p_b + p_g$, we may have $t = (p_b + p_W)^2/m_t^2$ significantly smaller than $t^* = (p_b + p_g + p_W)^2/m_t^2$. Without real-gluon emission, the invariant-mass cut defined above imposes a lower bound on the variable t , *i.e.* $t > y$ with $y = 1 - \Lambda^2/m_t^2$. With gluon emission from the bottom quark, the new variable t^* represents the quantity which before was described by the variable t . Then, for consistency, the lower cut has to be imposed on t^* , *i.e.* $t^* > y$. If, instead, we imposed a lower bound on t in the real-gluon case, the situation $t < y < t^*$ could arise, thus excluding events where the gluon is detected separately ($t < y$) and including events where the gluon is part of the bottom jet ($t^* > y$). Therefore, a collinear-safe observable is only obtained by imposing the lower limit on the variable t^* which corresponds to the 3-particle variable t when the collinear gluon is not detected separately in the detector. With this choice, we obtain integrals for the 4-particle phase space parametrized as

$$\int_y^1 dt^* \int_x^{t^*} dt. \quad (17)$$

To extract the endpoint behaviour, these integrals are asymptotically expanded for small $(1 - t^*)$, using the strategy of regions as explained in Sec. 3.1 below. In this param-

terization, the size of the variable $(t^* - t)$, which is proportional to the components of p_g , characterizes the different regions for expanding the inner integral in the limit $t^* \rightarrow 1$. We therefore need to keep track of factors of $(1 - t^*)$ and $(t^* - t)$ (or of $(1 - t) = (1 - t^*) + (t^* - t)$) appearing in the amplitudes. The phase-space splitting of the total momentum into p_{t^*} and the antitop momentum $p_{\bar{t}}$ provides a factor $(1 - t^*)^{1/2-\epsilon}$, and the gluon emission, $p_{t^*} \rightarrow p_t + p_g$, yields $(t^* - t)^{1-2\epsilon}$. Top propagators with momenta p_t and p_{t^*} contribute negative integer powers of $(1 - t)$ and $(1 - t^*)$, respectively, whereas bottom propagators with momentum $(p_b + p_g)$ and antitop propagators with momentum $(p_{\bar{t}} + p_g)$ have a negative power of $(t^* - t)$ each. Other possible propagators emerging from diagrams $h_1 - h_{10}$ after the addition of a gluon going through the cut are $\mathcal{O}(1)$ in the limit $t^* \rightarrow 1$, $t^* - t \rightarrow 0$. The overall scaling at leading order in $(1 - t^*)$ results as

$$\int_y^1 dt^* (1 - t^*)^{1/2-\epsilon-n_{t^*}} \int_x^{t^*} dt (t^* - t)^{1-2\epsilon-n_{b^*}-n_{\bar{t}^*}} (1 - t)^{-n_t} f(t), \quad (18)$$

where n_{t^*} , $n_{\bar{t}^*}$ and n_t are the numbers of top propagators with momenta $(p_t + p_g)$, $(p_{\bar{t}} + p_g)$ and p_t , respectively, n_{b^*} stands for the number of bottom propagators with momentum $(p_b + p_g)$, and $f(t)$ is a function of $\mathcal{O}(1)$ for $t \rightarrow 1$. Two different regions are identified for the inner t -integration: the hard region where $(t^* - t) \sim 1$, and the ultrasoft region where $(t^* - t) \sim (1 - t^*) \ll 1$. After performing the integral over t in the hard region and in the ultrasoft region, we obtain contributions with scalings $(1 - t^*)^{1/2-\epsilon-n_{t^*}}$ and $(1 - t^*)^{5/2-3\epsilon-n_{t^*}-n_{b^*}-n_{\bar{t}^*}-n_t}$, respectively, under the t^* -integral. Since the n 's are integer quantities, the endpoint-singular cases require either $n_{t^*} \geq 2$ or $n_{t^*} + n_{b^*} + n_{\bar{t}^*} + n_t \geq 4$. It is straightforward to check that these conditions are only accomplished by the real-gluon corrections to the NLO diagram h_1 , which consist of three squared $e^+e^- \rightarrow bW^+\bar{t}g$ diagrams and three interference diagrams, as shown in Fig. 4. Moreover, the amplitudes from Fig. 4 involve only endpoint-singular cases of the form $\int_y^1 dt^* (1 - t^*)^{-3/2-n\epsilon}$, producing contributions proportional to m_t/Λ according to (15). Subleading terms in the expansion in $(1 - t^*)$ do not yield half-integer powers, so no $1/\epsilon$ endpoint singularities arise from the real-gluon emission diagrams that contribute to the NNLO non-resonant cross section.

3.1 Calculation of endpoint singularities

The endpoint-singular contributions contained in the amplitudes of Figs. 3 and 4 arise from terms in the integrand of the outer phase-space integration of the form $(1 - t)^{r+n\epsilon}$, with $r = -2, -3/2, -1$ for the virtual-gluon corrections, and of the form $(1 - t^*)^{-3/2+n\epsilon}$ for the case of real-gluon emission. The extraction of such terms is greatly simplified if the 1-loop and phase-space integrals over other variables are asymptotically expanded in $(1 - t)$ and $(1 - t^*)$ prior to their evaluation using the strategy of expansion by regions [34–36]. The relevant regions are determined and their completeness is confirmed by asymptotically expanding Mellin–Barnes representations of the full integrals. Such an interplay between expansion by regions and Mellin–Barnes representations has been described in detail in [36]. For the 3-particle (virtual-gluon) diagrams, three regions

are found in the loop integration over the (gluon) momentum k : the *hard region* where $k \sim m_t$, the *ultrasoft region* where $k \sim m_t(1-t)$, and the *potential region* where $k^0 \sim m_t(1-t)$ and $\vec{k} \sim m_t(1-t)^{1/2}$ (defined in the rest frame of p_t). Note that these regions are analogous to the ones that are found in the threshold expansion [34] if we identify v^2 there with $(1-t)$. For the 4-particle (real-gluon) diagrams, only the hard region with $k \sim m_t(t^*-t) \sim m_t$ and the ultrasoft region with $k \sim m_t(t^*-t) \sim m_t(1-t^*)$ contribute to the phase-space integral over the variable t . It is illustrative to show how the method of regions applies to our case by means of two non-trivial examples.

Consider first the virtual gluon connecting the antitop with the on-shell bottom quark, diagram h_{1b} of Fig. 3. The relevant 1-loop scalar integral reads

$$\begin{aligned} I_{1b} &= \int d^d k \frac{1}{((p_t + k)^2 - m_t^2)((p_{\bar{t}} - k)^2 - m_t^2)(p_b + k)^2 k^2} \\ &= \int d^d k \frac{1}{(2p_t \cdot k + k^2 - m_t^2(1-t))(-2p_{\bar{t}} \cdot k + k^2)(2p_b \cdot k + k^2)k^2}, \end{aligned} \quad (19)$$

where we have used the on-shell conditions for the antitop ($p_{\bar{t}}^2 = m_t^2$) and the bottom quark ($p_b^2 = 0$). In order to expand the denominators for each region we need to know the scaling in $(1-t)$ of the final-state particle momenta. Working in the top rest frame, where $p_t = (p_t^0, \vec{0})$, simple kinematics gives, at leading order in $(1-t)$,

$$p_t^0 \simeq m_t, \quad p_{\bar{t}}^0 \simeq m_t, \quad |\vec{p}_{\bar{t}}| \simeq \sqrt{2}m_t(1-t)^{1/2}, \quad p_b^0 = |\vec{p}_b| \simeq \frac{m_t}{2}(1-x). \quad (20)$$

Note that we regard neither $(1-x)$ nor x as small quantities for the purpose of the $(1-t)$ -expansion. In the hard region where $k \sim m_t$, all the propagators scale as order $(1-t)^0$, and $I_{1b}^{(h)} \sim m_t^{-4-2\epsilon}(1-t)^0$. Taking into account the factor $(1-t)^{1/2-\epsilon}$ from the $q \rightarrow p_t + p_{\bar{t}}$ phase-space measure and $(1-t)^{-1}$ from the top propagator on the r.h.s. of the cut, the hard-region contribution scales as $(1-t)^{-1/2-\epsilon}$, and is thus endpoint-regular. In the ultrasoft region, we have to consider $k \sim m_t(1-t)$, which allows to drop k^2 from the fermion propagators as well as $\vec{p}_{\bar{t}} \cdot \vec{k}$, obtaining

$$I_{1b}^{(\text{us})} = \int d^d k \frac{1}{(2m_t k^0 - m_t^2(1-t))(-2m_t k^0)(2p_{b,0} \cdot k)k^2}, \quad (21)$$

where $p_{X,0}$ denotes the first term in the $t \rightarrow 1$ expansion of the corresponding momentum p_X . Therefore we get that $I_{1b}^{(\text{us})} \sim m_t^{-4-2\epsilon}(1-t)^{-1-2\epsilon}$, and an overall endpoint-singular contribution to diagram h_{1b} from the ultrasoft contribution scaling as $(1-t)^{-3/2-3\epsilon}$. An additional factor $\vec{p}_{\bar{t}} \cdot \vec{k}/(m_t k^0) \sim (1-t)^{1/2}$ in the integrand of $I_{1b}^{(\text{us})}$ (coming, for instance, from the next-to-leading term in the expansion of the antitop propagator in the ultrasoft region) could potentially yield a $1/\epsilon_{\text{ep}}$ endpoint divergence. However, the resulting angular integral can be shown to vanish, so there are no $1/\epsilon_{\text{ep}}$ endpoint divergences from the ultrasoft region.

Finally, the expansion of I_{1b} in the potential region where $k^0 \sim \vec{k}^2/m_t \sim (1-t)$ yields at leading order

$$I_{1b}^{(p)} = \int d^d k \frac{1}{(-\vec{k}^2 + 2m_t k^0 - m_t^2(1-t))(-\vec{k}^2 - 2m_t k^0 + 2\vec{p}_{\bar{t},0} \cdot \vec{k})(-2\vec{p}_{b,0} \cdot \vec{k})(-\vec{k}^2)}. \quad (22)$$

From (22) we find $I_{1b}^{(p)} \sim m_t^{-4-2\epsilon}(1-t)^{-1-\epsilon}$, and thus a leading-order scaling $(1-t)^{-3/2-2\epsilon}$ for the potential-region contribution to diagram h_{1b} . Subleading terms of order $(1-t)^{-1-2\epsilon}$ arise from the next-to-leading term in the expansion of the bottom propagator (suppressed by $(1-t)^{1/2}$) as well as from an additional factor of either $\vec{p}_{\bar{t},0} \cdot \vec{p}_{b,0}$ or $\vec{p}_{b,0} \cdot \vec{k}$ (both $\sim m_t^2(1-t)^{1/2}$) in the numerator of the full h_{1b} amplitude. These subleading terms generate the $1/\epsilon_{\text{ep}}$ endpoint divergences from diagram h_{1b} .

Let us now consider an example involving a real-gluon correction, namely diagram g_5 from Fig. 4. In the rest frames of either p_t or p_{t^*} , the components of the on-shell gluon momentum are proportional to the variable $(t^* - t)$, defined in Sec. 3, such that both the bottom propagator with momentum $(p_b + p_g)$ and the antitop propagator with momentum $(p_{\bar{t}} + p_g)$ provide a negative power of $(t^* - t)$ each. So, according to (18) with $n_{t^*} = n_{\bar{t}^*} = n_t = n_{b^*} = 1$, the integral over the variable t has the form

$$I_{g_5} = \int_x^{t^*} dt \frac{f(t)}{(1-t)(t^*-t)^{1+2\epsilon}} = \int_0^\infty du \frac{\theta(t^* - x - u) f(t^* - u)}{(1 - t^* + u) u^{1+2\epsilon}}, \quad (23)$$

where $f(t) \sim \mathcal{O}(1)$ for $t \rightarrow 1$, and we have introduced $u \equiv (t^* - t)$. Applying the expansion by regions to integrals with finite boundaries or theta functions is explained in [36]. We are interested in the expansion of this integral in $(1 - t^*)$. As can easily be confirmed by writing a Mellin–Barnes representation of the integral, for $t^* \rightarrow 1$ it receives contributions from the hard region, $u \sim 1 \gg 1 - t^*$, and from the ultrasoft region, $u \sim 1 - t^*$. In the former case we can expand out factors of $(1 - t^*)$ in the denominator of (23) and set $t^* \simeq 1$ in the numerator for the leading-order contribution:

$$I_{g_5}^{(h)} = \int_0^{1-x} du \frac{f(1-u)}{u^{2+2\epsilon}} \sim (1 - t^*)^0. \quad (24)$$

So the overall scaling of the hard contribution is given by the remaining factor in (18), $(1 - t^*)^{-1/2-\epsilon}$, which is endpoint-regular. However, in the ultrasoft region we have to set $\theta(t^* - x - u) \simeq \theta(1 - x) = 1$ and $f(t^* - u) \simeq f(1)$ and keep the first propagator unexpanded. Thus

$$I_{g_5}^{(\text{us})} = f(1) \int_0^\infty du \frac{1}{(1 - t^* + u) u^{1+2\epsilon}} \sim (1 - t^*)^{-1-2\epsilon}, \quad (25)$$

which provides the scaling $(1 - t^*)^{-3/2-3\epsilon}$ for the leading ultrasoft term. By explicit computation it can be shown that no $(1 - t^*)^{-1-3\epsilon}$ contribution is generated by subleading terms in the expansion of the ultrasoft region because they involve angular integrations of the form $\int_{-1}^{+1} d\cos\theta (1 - \cos^2\theta)^{-\epsilon} \cos\theta$ which vanish.

4 Results for the NNLO non-resonant contributions in the Λ/m_t expansion

The following results contain all endpoint-singular contributions to the individual diagrams in Figs. 3 and 4, *i.e.*, within the asymptotic expansion described above, the terms of (13) with $r \geq 1$. Endpoint-regular contributions with $r < 1$ are omitted. From the viewpoint of the results, all terms of the expansion in powers of Λ/m_t are provided up to and including the order $(\Lambda/m_t)^0 \ln(m_t^2/\Lambda^2)$, as shown in Eqs. (14)–(16). The omitted terms are of order $(\Lambda/m_t)^0$ without endpoint-singular $1/\epsilon$ terms or logarithms of Λ , or of higher order in (Λ/m_t) ; they are regular in the limit $\Lambda \rightarrow 0$. The results presented here get dominant in the limit $\Lambda \rightarrow 0$, where they are *a priori* not valid because our effective-field-theory treatment requires $\Lambda^2 \gg m_t \Gamma_t$ (see [28]). However, our result taking Λ as a tiny ($\Lambda \ll m_t$) unphysical scale provides a precise approximation of the amplitude at the endpoint, which could be complemented by a numerical evaluation of the contributions outside this tight Λ -cut (where the top propagators never go on shell) in order to get a precise evaluation of the full NNLO non-resonant corrections to the total cross section with or without invariant-mass cuts.

All the diagrams relevant to this NNLO analysis with the exception of h_{4a} have the structure of a hadronic tensor $H^{\mu\nu}$ connected to a leptonic tensor via two photon or Z propagators. While the leptonic tensor contains the e^+e^- pairs on the left-hand and right-hand sides of the forward-scattering amplitude, the hadronic tensor involves everything between the two photon/ Z propagators, including the cut through $bW^+\bar{t}(g)$, with the exception of two powers of the elementary charge e removed from the two external vertices. In the case of photon/ Z couplings to quarks, these two vertices on the left-hand and right-hand side of the hadronic tensor read

$$i\gamma^\mu (v_f^L - a_f^L \gamma_5) \quad \text{and} \quad i\gamma^\nu (v_f^R - a_f^R \gamma_5), \quad (26)$$

respectively, where $v_f^{L,R}$ and $a_f^{L,R}$ are the vector and axial-vector couplings of the corresponding quark ($f = t, b$). In the case of a Z -boson, they are given by

$$v_f^{L,R} = \frac{T_3^f - 2Q_f s_w^2}{2s_w c_w}, \quad a_f^{L,R} = \frac{T_3^f}{2s_w c_w}, \quad (27)$$

where s_w (c_w) is the sine (cosine) of the weak mixing angle, Q_f the electric charge of the fermion ($Q_t = 2/3$, $Q_b = -1/3$; similarly $Q_e = -1$), and T_3^f the third component of the weak isospin of the fermion. For a photon, $v_f^{L,R} = -Q_f$ and $a_f^{L,R} = 0$. In the case of diagram h_{3a} the relevant 3-gauge-boson coupling is I_{WW}^L , multiplying the usual momentum-dependent terms as defined in (49) below. We have $I_{WW}^L = 1$ for a photon attached to the left of the hadronic tensor and $I_{WW}^L = -c_w/s_w$ for a Z -boson.

We note that for all diagrams except for g_i , $i = 1, 2, 3$, (which are already symmetric) there is a symmetric contribution where the right and left parts of the diagram have been exchanged. For the diagrams with the hadronic-tensor structure (all except h_{4a}),

the corresponding amplitude for the symmetric amplitude is obtained by replacing the coupling factors on the sides of the hadronic tensor as

$$X^L Y^R \rightarrow Y^L X^R, \quad (28)$$

where $X, Y = v_t, a_t, v_b, a_b, I_{WW}$, and then taking the complex conjugate of the whole amplitude. The results in this section correspond to the amplitudes with $bW^+\bar{t}(g)$ cuts, as shown in Figs. 3 and 4. The additional diagrams with $\bar{b}W^-t(g)$ cuts also have to be taken into account when computing the non-resonant contribution to $e^+e^- \rightarrow W^+W^-b\bar{b}$, but their contribution is equal to the corresponding one with $bW^+\bar{t}(g)$ cuts by virtue of CP -invariance.

The hadronic tensor has the Lorentz structure $H^{\mu\nu} = H g^{\mu\nu} + \tilde{H} q^\mu q^\nu / q^2$ with the total momentum $q = p_{e^+} + p_{e^-} = p_b + p_W + p_{\bar{t}} (+p_g)$ and $q^2 = s$. Only the first term contributes to the cross section, it is projected out by

$$H = \frac{1}{3-2\epsilon} \left(g_{\mu\nu} - \frac{q_\mu q_\nu}{q^2} \right) H^{\mu\nu}. \quad (29)$$

For the propagators and polarization sums of gluons, Feynman gauge is used, while unitarity gauge is employed for W -bosons. All NNLO contributions are proportional to the factor

$$N_\epsilon = \left(\frac{\mu^2}{m_t^2} \right)^{3\epsilon} m_t \Gamma_t^{\text{Born}} N_c C_F \frac{\alpha_s}{4\pi}, \quad (30)$$

where μ is the scale introduced in dimensional regularization and $N_c = 3$ is the number of QCD colours. Γ_t^{Born} is the tree-level top decay width,

$$\Gamma_t^{\text{Born}} = \frac{\alpha |V_{tb}|^2 m_t (1-x)^2 (1+2x)}{16s_w^2 x}, \quad (31)$$

obtained from the amplitude $t \rightarrow bW^+$ with the bottom-quark mass set to zero. In the presentation of the results that follows, we shall mark if the $1/\epsilon$ poles are of ultraviolet, infrared or endpoint-singular origin by writing $1/\epsilon_{\text{UV}}$, $1/\epsilon_{\text{IR}}$ or $1/\epsilon_{\text{ep}}$, respectively.

4.1 Virtual corrections to diagram h_1

We first give results for the hadronic tensor coefficient H from the virtual $\mathcal{O}(\alpha_s)$ corrections to diagram h_1 , *i.e.* diagrams h_{1X} , $X = a, \dots, g$, depicted in Fig. 3, that generate the three types of endpoint-divergent contributions listed in (14)–(16). It is a general feature of these corrections that (m_t^2/Λ^2) and $(\Lambda/m_t)^0 \ln(m_t^2/\Lambda^2)$ terms arise only from the potential region in the 1-loop integration over the gluon momenta, whereas the (m_t/Λ) terms come from either hard or ultrasoft gluons (with the only exception of diagram h_{1b} , as explained below).

The amplitude for h_{1a} arises from inserting the virtual-gluon correction in the $t\bar{t}$ -vertex and has the highest degree of endpoint singularity, as explained in Sec. 3. The result reads

$$H_{1a} = N_\epsilon \left\{ 2 \frac{m_t^2}{\Lambda^2} v_t^L v_t^R + \frac{m_t}{\Lambda} v_t^L v_t^R \frac{\sqrt{2}}{\pi^2} \left[\frac{1}{\epsilon_{UV}} - 3 \ln \frac{m_t^2}{\Lambda^2} - 2 \ln(1-x) - \ln 2 + \frac{2(1+x)}{1+2x} \right] \right. \\ \left. + \left(\frac{1}{\epsilon_{ep}} + 2 \ln \frac{m_t^2}{\Lambda^2} \right) \left[-v_t^L v_t^R \frac{2(2+2x+5x^2)}{3(1-x)(1+2x)} - \frac{1}{4} v_t^L a_t^R + \frac{1}{6} a_t^L a_t^R \right] \right\}. \quad (32)$$

Terms of order $(\Lambda/m_t)^0$ without $1/\epsilon_{ep}$ terms or logarithms of Λ and endpoint-regular contributions of $\mathcal{O}(\Lambda/m_t)$ are omitted in our results, as explained above. Also terms of $\mathcal{O}(\epsilon)$ are dropped everywhere.

For the virtual gluon connecting the bottom and the antitop quark, diagram h_{1b} , the hadronic tensor coefficient reads

$$H_{1b} = N_\epsilon \left\{ \frac{m_t}{\Lambda} v_t^L v_t^R \frac{\sqrt{2}}{\pi^2} \left[-\frac{1}{\epsilon_{IR}^2} + \frac{1}{\epsilon_{IR}} \left(-3 \ln \frac{m_t^2}{\Lambda^2} + 2 \ln(1-x) + \ln 2 + \frac{2(1+3x)}{1+2x} \right) \right. \right. \\ \left. - \frac{9}{2} \ln^2 \frac{m_t^2}{\Lambda^2} + 3 \left(2 \ln(1-x) + \ln 2 + \frac{2(1+3x)}{1+2x} \right) \ln \frac{m_t^2}{\Lambda^2} \right. \\ \left. - 2 \ln^2(1-x) - 2 \left(\ln 2 + \frac{2(1+3x)}{1+2x} \right) \ln(1-x) - \frac{1}{2} \ln^2 2 \right. \\ \left. - \frac{2(1+3x)}{1+2x} \ln 2 - \frac{4(6+13x)}{1+2x} + \frac{\pi^2}{12} \right. \\ \left. + i\pi \left(-\frac{2}{\epsilon_{IR}} - 4 \ln \frac{m_t^2}{\Lambda^2} + 4 \ln(1-x) + \frac{4(1+3x)}{1+2x} \right) \right] \\ \left. + \left(\frac{1}{\epsilon_{ep}} + 2 \ln \frac{m_t^2}{\Lambda^2} \right) \left[v_t^L v_t^R \frac{3(1+x+2x^2)}{4(1-x)(1+2x)} - (v_t^L a_t^R - a_t^L v_t^R) \frac{1-2x}{6(1+2x)} \right] \right\}. \quad (33)$$

The single and double infrared singularities in (33) are related to the emission of the virtual gluon from the massless bottom quark. The contribution proportional to $i\pi$ of order m_t/Λ in the second-to-last line of (33) arises from potential-gluon momentum, but, as it is purely imaginary, it cancels with the symmetric contribution where the gluon is exchanged on the r.h.s. of the cut.

The virtual gluon correcting the tb -vertex, diagram h_{1c} , gives

$$H_{1c} = N_\epsilon \frac{m_t}{\Lambda} v_t^L v_t^R \frac{2\sqrt{2}}{\pi^2} \left[\frac{1}{2\epsilon_{UV}} + \frac{1}{\epsilon_{IR}} \left(\ln \frac{m_t^2}{\Lambda^2} + \ln(1-x) - 3 \right) \right. \\ \left. + 2 \ln^2 \frac{m_t^2}{\Lambda^2} - \left(\ln(1-x) + \ln 2 + \frac{9+22x}{2(1+2x)} \right) \ln \frac{m_t^2}{\Lambda^2} \right]$$

$$\begin{aligned}
& -3 \ln^2(1-x) + \left(\frac{7+15x}{1+2x} - \ln 2 \right) \ln(1-x) + \frac{5}{2} \ln 2 \\
& + \frac{5(1+3x)}{1+2x} - \text{Li}_2(x) + \frac{\pi^2}{6} \Big]. \tag{34}
\end{aligned}$$

The remaining virtual corrections to diagram h_1 correspond to renormalization and self-energy contributions. At $\mathcal{O}(\alpha_s)$, the top- and bottom-quark fields and the top mass need to be renormalized, which is done in the on-shell scheme. Since the non-resonant NLO diagrams are purely of electroweak origin, they do not involve QCD couplings, so the renormalization of α_s is irrelevant for the current NNLO analysis. The insertion of the renormalized self-energy into a top/antitop line with momentum p next to a cut vanishes, since this contribution is proportional to $(m_t^2 - p^2)^{-2\epsilon}$ in the on-shell limit, and the Cutkosky rules prescribe a factor $\delta(p^2 - m^2)$ which sets $(m_t^2 - p^2)^{-2\epsilon}$ to zero as a scaleless term in dimensional regularization. The same is true for a cut bottom line, because the bottom self-energy is scaleless and vanishes for $p_b^2 = 0$. Therefore we do not need to consider self-energy insertions in lines which are cut. On the other hand, when the top self-energy is inserted into an internal top line, the top-field renormalization parts of the vertex counterterms from the two adjacent vertices cancel exactly the contribution of the field-renormalization to the 2-point top counterterm in the renormalized self-energy insertion, so the complete correction to an internal top line is equal to the insertion of the bare self-energy plus the mass-renormalization part of the 2-point top counterterm. This correction only generates an endpoint-singular contribution when inserted into the internal top lines of the NLO diagram h_1 . The corresponding NNLO diagrams are h_{1d} and h_{1e} in Fig. 3, and the sum of both gives the coefficient

$$H_{1de} = N_\epsilon \frac{m_t}{\Lambda} v_t^L v_t^R \frac{\sqrt{2}}{\pi^2} \left[-\frac{1}{\epsilon_{\text{UV}}} + 3 \ln \frac{m_t^2}{\Lambda^2} + 2 \ln(1-x) + \ln 2 - \frac{2(5+9x)}{1+2x} \right]. \tag{35}$$

The bare self-energy entering diagram h_{1d} receives contributions from hard and ultrasoft loop momenta, whereas the mass- as well as the field-renormalization constants are entirely determined by hard contributions. For the computation of h_{1e} (and also for h_{1f} and h_{1g}) we need the result for the NLO amplitude h_1 retaining $\mathcal{O}(\epsilon)$ terms, which was not necessary for the calculation performed in [28]. For completeness we write here the hadronic tensor coefficient for the endpoint-singular term of h_1 with the full ϵ -dependence:

$$H_1^{\text{NLO}} = \left(\frac{\mu^2}{m_t^2} \right)^{2\epsilon} m_t \Gamma_t^{\text{Born}} N_c v_t^L v_t^R \frac{m_t}{\Lambda} \frac{2^{1/2-\epsilon} e^{2\epsilon\gamma_E} \Gamma^2(1-\epsilon)}{\pi^2 (1+2\epsilon) \Gamma^2(2-2\epsilon)} \frac{1+2(1-\epsilon)x}{(1+2x)(1-x)^{2\epsilon}} \left(\frac{m_t^2}{\Lambda^2} \right)^\epsilon. \tag{36}$$

Although the renormalized self-energy insertion into a cut bottom line vanishes, there is a contribution from the bottom-field renormalization part $\delta_b/2$ of the counterterm of the tbW vertex, diagram h_{1f} . This correction is obtained by multiplying the NLO

result H_1^{NLO} (36) with $\delta_b/2$, where δ_b is defined from the relation between the bare and renormalized bottom-quark field, $b_0 = (1 + \delta_b)^{1/2}b$,

$$\delta_b = \left(\frac{\mu^2}{m_t^2}\right)^\epsilon C_F \frac{\alpha_s}{4\pi} \left(-\frac{1}{\epsilon_{\text{UV}}} + \frac{1}{\epsilon_{\text{IR}}}\right) + \mathcal{O}(\alpha_s^2), \quad (37)$$

obtaining

$$H_{1f} = N_\epsilon \frac{m_t}{\Lambda} v_t^L v_t^R \frac{\sqrt{2}}{\pi^2} \left(-\frac{1}{2\epsilon_{\text{UV}}} + \frac{1}{2\epsilon_{\text{IR}}}\right), \quad (38)$$

which is effectively zero, but exhibits separate ultraviolet and infrared singularities.

Finally, there is a contribution from top-field renormalization, diagram h_{1g} , attributed to the antitop part $\delta_t/2$ of the counterterm of the $t\bar{t}$ -vertex. The top-field counterterm δ_t , defined analogously to δ_b , is determined from the derivative of the bare self-energy with respect to \not{p}_t , giving

$$\delta_t = \left(\frac{\mu^2}{m_t^2}\right)^\epsilon C_F \frac{\alpha_s}{4\pi} \left(-\frac{1}{\epsilon_{\text{UV}}} - \frac{2}{\epsilon_{\text{IR}}} - 4\right) + \mathcal{O}(\alpha_s^2). \quad (39)$$

Multiplying $\delta_t/2$ with (36) we get for the hadronic tensor coefficient from diagram h_{1g} :

$$H_{1g} = N_\epsilon \frac{m_t}{\Lambda} v_t^L v_t^R \frac{\sqrt{2}}{\pi^2} \left[-\frac{1}{2\epsilon_{\text{UV}}} - \frac{1}{\epsilon_{\text{IR}}} - \frac{3}{2} \ln \frac{m_t^2}{\Lambda^2} + 3 \ln(1-x) + \frac{3}{2} \ln 2 - \frac{5+7x}{1+2x} \right]. \quad (40)$$

Let us note that in the sum of all virtual-gluon corrections and renormalization contributions to the diagram h_1 listed above, the ultraviolet $1/\epsilon_{\text{UV}}$ singularities cancel out, such that the overall $\mathcal{O}(\alpha_s)$ correction is ultraviolet-finite. (Recall that the $1/\epsilon$ divergences in the real-gluon corrections discussed next can only be of infrared origin.)

4.2 Real-gluon corrections

As explained in Sec. 3, for endpoint-singular contributions involving real gluons we need to consider only the forward-scattering amplitudes with a 4-particle cut corresponding to real-gluon corrections to the NLO diagram h_1 . These have been shown explicitly in Fig. 4 for the case of $bW^+\bar{t}g$ cuts. The real-gluon corrections involve three squared $e^+e^- \rightarrow bW^+\bar{t}g$ amplitudes (diagrams g_1, g_2, g_3) and three interference amplitudes (diagrams g_4, g_5, g_6) that have a symmetric counterpart which is obtained by mirroring the diagram across the cut (without reversing the fermion flow).

The contributions to the hadronic tensor from the symmetric diagrams read

$$H_{g_1} = N_\epsilon \frac{m_t}{\Lambda} v_t^L v_t^R \frac{\sqrt{2}}{\pi^2} \left[-4 \left(\ln \frac{m_t^2}{\Lambda^2} + \ln(1-x) \right) + \frac{x^2 (3+10x)}{(1-x)^2 (1+2x)} \ln x \right. \\ \left. + \frac{109+85x-116x^2}{6(1-x)(1+2x)} \right], \quad (41)$$

$$H_{g_2} = N_\epsilon \frac{m_t}{\Lambda} v_t^L v_t^R \frac{\sqrt{2}}{\pi^2} \left[-\frac{1}{\epsilon_{\text{IR}}} - \ln \frac{m_t^2}{\Lambda^2} + 4 \ln(1-x) + \ln 2 + \frac{x^2 (3-2x)}{(1-x)^2 (1+2x)} \ln x - \frac{29+5x-40x^2}{6(1-x)(1+2x)} \right], \quad (42)$$

$$H_{g_3} = N_\epsilon \frac{m_t}{\Lambda} v_t^L v_t^R \frac{2\sqrt{2}}{\pi^2} \left[\frac{1}{\epsilon_{\text{IR}}} + 3 \ln \frac{m_t^2}{\Lambda^2} - 2 \ln(1-x) - \ln 2 + \frac{2(1+x)}{1+2x} \right]. \quad (43)$$

While diagram g_1 receives contributions from both hard and ultrasoft gluons, diagram g_2 only gets contributions from the hard region and diagram g_3 only from the ultrasoft region.

In the case of the interference diagrams, the contributions of both g_4 and g_5 are entirely produced by ultrasoft gluons, whereas g_6 receives as well contributions from hard gluons. The results for the interference diagrams read

$$H_{g_4} = -N_\epsilon \frac{m_t}{\Lambda} v_t^L v_t^R \frac{4\sqrt{2}}{\pi^2}, \quad (44)$$

$$\begin{aligned} H_{g_5} = N_\epsilon \frac{m_t}{\Lambda} v_t^L v_t^R \frac{\sqrt{2}}{\pi^2} & \left[\frac{1}{\epsilon_{\text{IR}}} + \frac{1}{\epsilon_{\text{IR}}} \left(3 \ln \frac{m_t^2}{\Lambda^2} - 2 \ln(1-x) - \ln 2 - \frac{2(1+3x)}{1+2x} \right) \right. \\ & + \frac{9}{2} \ln^2 \frac{m_t^2}{\Lambda^2} - 3 \left(2 \ln(1-x) + \ln 2 + \frac{2(1+3x)}{1+2x} \right) \ln \frac{m_t^2}{\Lambda^2} \\ & + 2 \ln^2(1-x) + 2 \left(\ln 2 + \frac{2(1+3x)}{1+2x} \right) \ln(1-x) + \frac{1}{2} \ln^2 2 \\ & \left. + \frac{2(1+3x)}{1+2x} \ln 2 + \frac{4(6+13x)}{1+2x} - \frac{\pi^2}{12} \right], \quad (45) \end{aligned}$$

$$\begin{aligned} H_{g_6} = N_\epsilon \frac{m_t}{\Lambda} v_t^L v_t^R \frac{2\sqrt{2}}{\pi^2} & \left[\frac{1}{\epsilon_{\text{IR}}} \left(-\ln \frac{m_t^2}{\Lambda^2} - \ln(1-x) + 3 \right) - 2 \ln^2 \frac{m_t^2}{\Lambda^2} \right. \\ & + \left(\ln(1-x) + \ln 2 + \frac{5+12x}{1+2x} \right) \ln \frac{m_t^2}{\Lambda^2} + 3 \ln^2(1-x) \\ & + \left(\ln 2 - \frac{2(5+9x)}{1+2x} \right) \ln(1-x) - 3 \ln 2 - \frac{x(2+x) \ln x}{2(1-x)^2(1+2x)} \\ & \left. - \frac{43+97x-122x^2}{12(1-x)(1+2x)} + \text{Li}_2(1-x) - \frac{2\pi^2}{3} \right]. \quad (46) \end{aligned}$$

It can be checked that in the sum of the real-gluon and virtual-gluon corrections to diagram h_1 , the infrared-singular terms cancel out completely. The cancellation of

infrared divergences holds independently for the combinations $h_{1b} + g_5$, $h_{1c} + g_6$, $2h_{1f} + g_2$ and $2h_{1g} + g_3$, where the factor 2 in front of h_{1f} and h_{1g} accounts for the symmetric contribution. It is also interesting to note that the sum of the ultrasoft-gluon (real and virtual) contributions in the $\mathcal{O}(\alpha_s)$ corrections to diagram h_1 above vanishes. In particular, the ultrasoft pieces in the combinations $h_{1a} + h_{1d} + h_{1e}$, $h_{1b} + g_5$, $h_{1c} + g_6$ and $g_1 + g_3 + 2g_4$, cancel out separately. Since there are no potential-region contributions of order m_t/Λ and the remaining endpoint-singular diagrams h_{ia} , $i = 2, 3, 4$, give only $(\Lambda/m_t)^0 \ln(m_t^2/\Lambda^2)$ terms, the order m_t/Λ in the non-resonant cross section originates purely from the hard region. This also implies that logarithms $\ln(m_t^2/\Lambda^2)$ will be absent in the m_t/Λ term: In individual contributions, they arise from expanding hard-region terms $\epsilon^{-k} (m_t^2/\Lambda^2)^\epsilon$ and ultrasoft-region terms $\epsilon^{-k} (m_t^2/\Lambda^2)^{3\epsilon}$ in powers of ϵ . Due to the different scaling of these two regions with m_t^2/Λ^2 , logarithms $\ln(m_t^2/\Lambda^2)$ may remain in a contribution even if it is finite for $\epsilon \rightarrow 0$, cf. the amplitude (41) for diagram g_1 . But where the contributions from both hard and ultrasoft regions are separately finite or, as here, the ultrasoft contribution vanishes completely, leaving only an ultraviolet- and infrared-finite hard contribution, there the logarithms $\ln(m_t^2/\Lambda^2)$ must disappear.

The cancellation of ultrasoft terms in the NNLO non-resonant calculation is closely connected with the absence of contributions from ultrasoft gluons in the NNLO matrix element (2) containing the interactions among the resonant top and antitop quarks. We postpone the discussion of this issue to Sec. 5.1.

4.3 Virtual corrections to diagrams h_2, h_3, h_4

The NNLO diagrams h_{2a} , h_{3a} and h_{4a} of Fig. 3 produce endpoint-singular contributions of the form (16). The additional power $(1-t)^{-1/2-\epsilon}$ needed to produce the $1/\epsilon_{\text{ep}}$ from the NLO diagrams h_2 , h_3 and h_4 arises from the potential region of the $t\bar{t}$ -vertex correction. The hadronic tensor coefficients from h_{2a} and h_{3a} read

$$H_{2a} = N_\epsilon v_t^L (v_b^R + a_b^R) \frac{1 - 5x - 2x^2}{12(1+x)(1+2x)} \left(\frac{1}{\epsilon_{\text{ep}}} + 2 \ln \frac{m_t^2}{\Lambda^2} \right), \quad (47)$$

$$H_{3a} = -N_\epsilon I_{WW}^L v_t^R \frac{2 + 5x - 2x^2}{12x(1+2x)} \left(\frac{1}{\epsilon_{\text{ep}}} + 2 \ln \frac{m_t^2}{\Lambda^2} \right), \quad (48)$$

where the coupling factor I_{WW}^L in (48) is defined from the 3-gauge-boson vertex Feynman rule

$$i I_{WW}^L \left[g^{\mu\rho} (q + p_{W^-})^\sigma + g^{\rho\sigma} (-p_{W^-} + p_{W^+})^\mu + g^{\sigma\mu} (-p_{W^+} - q)^\rho \right], \quad (49)$$

omitting the elementary charge e . The total momentum $q = p_{W^+} + p_{W^-}$ is incoming from the left-hand side (index μ), the lower W^- -boson has outgoing momentum p_{W^-} (index ρ), and the upper W^+ -boson has outgoing momentum p_{W^+} (index σ).

For diagram h_{4a} we have to evaluate directly its contribution to the unpolarized $e^+e^- \rightarrow bW^+\bar{t}$ cross section, since it does not have the structure of a hadronic tensor contracted with a leptonic tensor. The cross-section contribution of diagram h_{4a} , already

summed over the two gauge bosons, photon and Z , in the s -channel propagator reads

$$\Delta\sigma_{4a} = -N_\epsilon \frac{\pi^2 \alpha^2}{s_w^2} \frac{1}{s} \left(\frac{Q_t Q_e}{s} + \frac{v_t(v_e + a_e)}{s - M_Z^2} \right) \frac{x}{(1-x)^3(1+2x)} \\ \times \left[4 \ln \left(\frac{2}{x} - 1 \right) + \frac{(1-x)(1-2x-23x^2)}{3x^2} \right] \left(\frac{1}{\epsilon_{\text{ep}}} + 2 \ln \frac{m_t^2}{\Lambda^2} \right), \quad (50)$$

where the squared centre-of-mass energy s has been set to $4m_t^2$ only in the non-trivial parts of the loop and phase-space integrations, but kept general in the photon and Z propagators and in the kinematic factors of the cross section. This corresponds to the same prescription used for the NLO non-resonant contributions computed in [28].

4.4 Complete endpoint-singular NNLO non-resonant cross section

With all the results from the individual diagrams of Figs. 3 and 4 at hand, we can compute the complete endpoint-singular non-resonant NNLO contribution to the $e^+e^- \rightarrow W^+W^-b\bar{b}$ cross section.

First, we need to sum up the contributions which come in the form of a hadronic tensor coefficient (all diagrams except h_{4a}). The real-gluon contributions H_{g_1} (41), H_{g_2} (42) and H_{g_3} (43) from symmetric diagrams have to be counted once. For all other diagrams, there are corresponding symmetric diagrams, so the virtual-gluon contributions H_{1a} (32), H_{1b} (33), H_{1c} (34), H_{2a} (47) and H_{3a} (48), the renormalization and self-energy contributions H_{1de} (35), H_{1f} (38) and H_{1g} (40), and the real-gluon interference contributions H_{g_4} (44), H_{g_5} (45) and H_{g_6} (46) have to be symmetrized before adding them together. This is done by replacing pairs of coupling factors as specified in (28). The contribution of each diagram (with hadronic tensor coefficient H) to the unpolarized $e^+e^- \rightarrow bW^+\bar{t}(g)$ cross section is then given by

$$\Delta\sigma = -8(1-\epsilon)\pi^2 \alpha^2 \frac{v_e^L v_e^R + a_e^L a_e^R}{(s - M_L^2)(s - M_R^2)} H, \quad (51)$$

where α is the electromagnetic coupling and M_L and M_R are the masses of the gauge bosons to the left-hand and right-hand sides of the hadronic tensor; the latter are attached to the e^+e^- initial state via couplings $v_e^{L,R}$ and $a_e^{L,R}$, defined analogously to (26). The contribution (51) has to be summed over the four combinations of gauge bosons (L, R = photon, Z) and, in addition, it must be counted twice, because for every contribution with $bW^+\bar{t}(g)$ cut presented here, an equivalent one with $\bar{b}W^-t(g)$ cut exists.

The result from the correction $\Delta\sigma_{4a}$ (50) must be counted four times (symmetrization and counting both cuts $bW^+\bar{t}$ and $\bar{b}W^-t$). After adding this piece, the following complete endpoint-singular non-resonant NNLO contribution to the cross section results:

$$\begin{aligned}
\sigma_{\text{non-res}}^{(2),\text{ep}} &= \frac{32\pi^2\alpha^2}{s} \frac{\Gamma_t^{\text{Born}}}{m_t} N_c \\
&\times \left\{ \left[Q_t^2 C_{\gamma\gamma}(s) - 2Q_t v_t C_{\gamma Z}(s) + v_t^2 C_{ZZ}(s) \right] \left\{ 2C_F \frac{\alpha_s}{\pi} \frac{m_t^2}{\Lambda^2} \right. \right. \\
&\quad \left. \left. + \frac{2\sqrt{2}}{\pi^2} \frac{m_t}{\Lambda} \left(\delta\Gamma_t^{(1)} - 4C_F \frac{\alpha_s}{\pi} \right) \right\} \right. \\
&\quad + \left\{ - \left[Q_t^2 C_{\gamma\gamma}(s) - 2Q_t v_t C_{\gamma Z}(s) + v_t^2 C_{ZZ}(s) \right] \frac{7+7x+22x^2}{6(1-x)(1+2x)} \right. \\
&\quad + \frac{1}{3} a_t^2 C_{ZZ}(s) + \frac{1}{2} Q_t a_t C_{\gamma Z}(s) - \frac{1}{2} v_t a_t C_{ZZ}(s) \\
&\quad + \left[Q_t Q_b C_{\gamma\gamma}(s) - (Q_t(v_b + a_b) + Q_b v_t) C_{\gamma Z}(s) + v_t(v_b + a_b) C_{ZZ}(s) \right] \\
&\quad \times \frac{1-5x-2x^2}{6(1+x)(1+2x)} \\
&\quad + \left[Q_t C_{\gamma\gamma}(s) - \left(v_t + Q_t \frac{c_w}{s_w} \right) C_{\gamma Z}(s) + v_t \frac{c_w}{s_w} C_{ZZ}(s) \right] \frac{2+5x-2x^2}{6x(1+2x)} \\
&\quad - \left[Q_t C_{\gamma}(s) + v_t C_Z(s) \right] \left[\ln\left(\frac{2}{x} - 1\right) + \frac{(1-x)(1-2x-23x^2)}{12x^2} \right] \\
&\quad \left. \left. \times \frac{x}{4(1-x)^3(1+2x)} \right\} C_F \frac{\alpha_s}{2\pi} \left(\frac{1}{\epsilon_{\text{ep}}} + 2 \ln \frac{\mu_{\text{soft}}^2}{\Lambda^2} \right) \right\}, \tag{52}
\end{aligned}$$

where we have used the functions

$$\begin{aligned}
C_{\gamma\gamma}(s) &= -Q_e^2 \frac{m_t^2}{4s}, & C_{\gamma Z}(s) &= \frac{Q_e v_e m_t^2}{4(s - M_Z^2)}, & C_{ZZ}(s) &= -\frac{(v_e^2 + a_e^2) m_t^2 s}{4(s - M_Z^2)^2}, \\
C_{\gamma}(s) &= \frac{Q_e m_t^2}{s_w^2 s}, & C_Z(s) &= \frac{(v_e + a_e) m_t^2}{s_w^2 (s - M_Z^2)}, \tag{53}
\end{aligned}$$

which arise from the photon and Z -boson propagators, and dropped $\mathcal{O}(\epsilon)$ terms. In order to improve the quality of the EFT expansion, we have kept $q^2 = s$ general in all photon and Z propagators as well as in the kinematic factors of the cross section and set $s = 4m_t^2$ only in the non-trivial parts of the loop and phase-space integrations, as done in [28]. We comment below on the introduction of the scale μ_{soft} in (52).

The coefficient $\delta\Gamma_t^{(1)}$ in the m_t/Λ term of (52) is equal to

$$\delta\Gamma_t^{(1)} = C_F \frac{\alpha_s}{2\pi} \left[- \left(2 \ln x + \frac{5+4x}{1+2x} \right) \ln(1-x) - 4 \text{Li}_2(x) - \frac{2\pi^2}{3} - \frac{2x(1+x)(1-2x)}{(1-x)^2(1+2x)} \ln x + \frac{5+9x-6x^2}{2(1-x)(1+2x)} \right], \quad (54)$$

which agrees with the first-order QCD correction to the top decay width neglecting the bottom mass, first obtained in [37]. $\delta\Gamma_t^{(1)}$ is given by the sum of the hard-region contributions from diagrams h_{1c} , h_{1f} , g_1 , g_2 , g_6 and from one half of $h_{1d} + h_{1e}$. The hard-region contribution from diagrams h_{1d} and h_{1e} is actually equal to the top-field renormalization contribution from the counterterms of both vertices adjacent to the top line ($2 \times \delta_t/2$ multiplied with the NLO diagram h_1). The above-mentioned set of diagrams provides virtual and real corrections which only affect the upper top line. In the on-shell top case which is effectively taken by the leading hard-region contribution, these corrections precisely correspond to the $\mathcal{O}(\alpha_s)$ corrections to the on-shell decay process $t \rightarrow bW^+$. In the result (52), $\delta\Gamma_t^{(1)}$ multiplies exactly the endpoint-divergent $\Gamma_t^{\text{Born}}/\Lambda$ term in the NLO non-resonant result of [28], such that $\delta\Gamma_t^{(1)}$ may be dropped from our NNLO result if the top width in the NLO result is replaced by its α_s -corrected version $\Gamma_t^{\text{Born}}(1 + \delta\Gamma_t^{(1)})$.

Eq. (52) is the main result of this work. As mentioned before, all ultraviolet ($1/\epsilon_{\text{UV}}$) and infrared ($1/\epsilon_{\text{IR}}$) singularities are canceled (independently of each other) in this total contribution. The only remaining poles are found at order $(\Lambda/m_t)^0$; they represent $1/\epsilon_{\text{ep}}$ endpoint singularities and originate purely from the potential region. When the $1/\epsilon$ finite-width divergences (10) from the NNLO resonant contributions in NRQCD are added to the NNLO non-resonant result (52), we observe a total cancellation of the $1/\epsilon$ divergences.² For the cancellation of the dependence on the renormalization scale $\mu_{\text{soft}} \sim m_t v$ associated with the finite-width divergences we have replaced consistently

$$\left(\frac{\mu^2}{m_t^2} \right)^{3\epsilon} \rightarrow \left(\frac{\mu_{\text{hard}}^2}{m_t^2} \right)^\epsilon \left(\frac{\mu_{\text{soft}}^2}{m_t^2} \right)^{2\epsilon} \quad (55)$$

in the NNLO non-resonant amplitudes and taken $\mu_{\text{hard}} = m_t$. This is justified by the fact that our $1/\epsilon_{\text{ep}}$ singularities originate from one hard integration (associated with the decay $t \rightarrow bW^+$) and two integrations with contributions from a smaller scale $\mu_{\text{soft}} \ll \mu_{\text{hard}}$, stemming from the on-shell limit of the top quarks and from potential-region gluon momenta. Also in the resonant NNLO amplitude, one of the subgraphs always corresponds to a hard contribution, *i.e.* to a matching coefficient between QCD and NRQCD which is evaluated with $\mu_{\text{hard}} = m_t$ (and in $d = 4$ dimensions). By setting consistently $\mu_{\text{hard}} = m_t$ in our contributions, too, the explicit dependence on μ_{soft} associated with the top-quark instability in the NNLO resonant contributions (*i.e.* the $\log \mu_{\text{soft}}$ terms

²We have to set $s = 4m_t^2$ and $M_Z^2 = m_t^2 x/c_w^2$, as done in the calculation of the absorptive matching coefficients $C_p^{(v/a),\text{abs}}$ [31], in order to find an exact cancellation.

proportional to Γ_t or $C_p^{(v/a),\text{abs}}$) cancels against the μ_{soft} -dependence of the NNLO non-resonant endpoint-singular contributions (52), together with the cancellation of the $1/\epsilon$ poles. The remaining logarithms of kinematic scales in this combination of resonant and non-resonant pieces for the inclusive $t\bar{t}$ cross section with bW invariant-mass cuts are of the form $\log(m_tv/\Lambda)$, in addition to logarithms of the velocity in the resonant EFT matrix elements.

5 Comparison with other approaches

5.1 Comparison with the phase-space matching approach

Our result (52) for the non-resonant contributions to the total cross section with an invariant-mass cut Λ^2 on the bW subsystems was obtained for the case of loose cuts, $\Lambda^2 \gg m_tE \sim m_t\Gamma_t$. The condition of loose cuts implies that the invariant-mass constraint only enters in the computation of the non-resonant contributions, while matrix elements on the resonant side are unaffected, as explained in Refs. [28, 38]. The endpoint-divergent terms presented here are equivalent to the first terms in the expansion in Λ/m_t of the full NNLO non-resonant result.

Interestingly enough, an alternative approach [30] (named *phase-space matching*) has determined the matching coefficients of the four-electron operators providing the non-resonant contributions to the cross section with invariant-mass cuts on the bW pairs in the same range, $m_t\Gamma_t \ll \Lambda^2 \ll m_t^2$, but through calculations involving only the matrix elements in the non-relativistic effective theory. In the phase-space matching (PSM) approach, symmetric cuts on the invariant masses of the top and antitop decay products restrict the integration over the top and antitop momenta in the resonant diagrams contributing to (2). Then the resulting cut integrals are expanded assuming that $\Lambda^2 \gg m_t\Gamma_t$, but still smaller than m_t^2 so that the non-relativistic expansion carried out by NRQCD is still valid, yielding

$$C(\alpha_s) \times \frac{\Gamma_t}{\Lambda} \times \sum_{n,m,k=0} \left[\left(\frac{m_t\Gamma_t}{\Lambda^2} \right)^n \times \left(\frac{\Lambda^2}{m_t^2} \right)^m \right] \left(\alpha_s \frac{m_t}{\Lambda} \right)^k + \sigma_{\text{NRQCD}}(\infty), \quad (56)$$

where $\sigma_{\text{NRQCD}}(\infty)$ is the NRQCD resonant cross section without invariant-mass restrictions (equivalently, for $\Lambda \rightarrow \infty$). The first term in (56) with powers of Λ can be understood as minus the contributions to the NRQCD matrix elements from the regions where the invariant-mass constraints are not fulfilled, which are then subtracted from the unrestricted cross section by means of (56). The powers of Λ^2/m_t^2 in (56) arise from cut diagrams with relativistic corrections, while factors of $\alpha_s m_t/\Lambda$ are introduced by cut diagrams with Coulomb-like gluons. $C(\alpha_s) = C_0 + C_1\alpha_s + \dots$ is a hard coefficient coming, for instance, from the matching of the vector current that produces the non-relativistic $t\bar{t}$. Assuming for the power-counting that $\Lambda \sim \mathcal{O}(m_t)$, the NLO terms in the phase-space matching approach correspond to the terms $n = k = 0$ in (56) with $C(\alpha_s) \simeq C_0$, while at NNLO we have to retain those with $n = 0$ and $k = 1$ plus the

$\mathcal{O}(\alpha_s)$ correction to $C(\alpha_s)$ times the NLO term. The whole computation is equivalent to the non-relativistic expansion of the full-theory squared matrix elements containing the double-resonant diagrams for $e^+e^- \rightarrow t\bar{t} \rightarrow W^+W^-b\bar{b}$ and their interference with the diagrams for $e^+e^- \rightarrow W^+W^-b\bar{b}$ having only either the top or the antitop in intermediate stages. However, the full-theory contributions coming from the square of single-top and pure background diagrams (the so-called remainder contributions in [30]) cannot be reproduced by EFT resonant diagrams, and thus have to be computed with external tools in the phase-space matching approach. For moderate invariant-mass cuts it was shown in [30] through a numerical comparison with the full-theory tree-level $e^+e^- \rightarrow W^+W^-b\bar{b}$ cross section that the remainder contributions are small at NLO. Indeed, in the computation of non-resonant corrections at this order within the unstable-particle EFT (*i.e.* the $n = k = 0$ terms in (56)), the remainder contributions are reproduced by diagrams $h_5 - h_{10}$ (see Fig. 2) that contribute first with $\Gamma_t \Lambda^3/m_t^4$ terms in the Λ/m_t -expansion, corresponding to $m = 2$ in (56). For the first two NLO terms in the series of (56), $m = 0, 1$, it was checked in [28] that they agree with the corresponding terms in the expansion of the full NLO non-resonant result.

Under the assumption that the QCD corrections to the remainder contributions are also small in the above-mentioned range of invariant-mass cuts, the phase-space matching contributions at $\mathcal{O}(\alpha_s)$ were also computed in [30]. We can now compare the NNLO terms of the phase-space matching series with those computed in this work, Eq. (52): the same coefficients in the m_t^2/Λ^2 , m_t/Λ and $(m_t/\Lambda)^0 \log \Lambda$ contributions are found from that comparison.³

A simple argument can be used to explain why the two methods yield the same series expansion in (Λ/m_t) of the non-resonant contributions, despite the different starting points in the respective calculations. In our method, the full-theory amplitude is expanded first assuming that top-quark lines are off-shell, *i.e.* $|p_t^2 - m_t^2| \sim m_t^2$, which drops the top self-energy corrections from the full-theory top-quark propagator, and then the (Λ/m_t) series arises from further expanding the resulting amplitude around the on-shell limit, *i.e.* for $|p_t^2 - m_t^2| \ll m_t^2$. The last expansion is equivalent to considering that the momentum p_t is potential, since the antitop on-shell condition sets $p_t^0 - m_t = (p_t^2 - m_t^2)/(4m_t) \sim \vec{p}_t^2/m_t \ll m_t$. On the other side, the PSM computation starts from the full-theory amplitude expanded for nearly on-shell (potential) top quarks, with $p_t^0 - m_t \sim \vec{p}_t^2/m_t \sim m_t v^2$, producing \vec{p}_t^2/m_t^2 and $(p_t^0 - m_t)/m_t$ corrections. Then the latter are transformed into (Λ^2/m_t^2) terms from hard- p_t momentum regions ($|p_t^2 - m_t^2| \sim m_t^2$) where we can expand the integrand taking the off-shellness of p_t much larger than the non-relativistic scales Γ_t and E . The first important observation is that in both methods a double expansion of the integrand in p_t (according to hard and poten-

³We note that in the phase-space matching approach, the term $m_t/\Lambda \times \delta\Gamma_t^{(1)}$ in (52) is generated by including in the NRQCD top-quark propagators the $\mathcal{O}(\alpha_s)$ corrections to the top width, which was not done explicitly in the analysis of [30] because Γ_t was considered an input parameter there. The rest of the m_t/Λ correction in (52) arises in the phase-space matching approach from the product of the $\mathcal{O}(\alpha_s)$ correction to the vector-current matching coefficient $(-2C_F \alpha_s/\pi)$ at both $t\bar{t}$ -vertices with the NLO phase-space matching contributions.

tial region scalings) is performed, but in reversed order. In the method of regions, such double expansions are known as overlap contributions [36]. Adopting the notation of the latter reference, we can denote as $T^{(p)}T^{(h)}I$ the integrand resulting from expanding the full-theory integrand I (including the Dirac delta functions from the Cutkosky rules) according to first hard and then potential momentum, and $T^{(h)}T^{(p)}I$ the same expansion taken in the reversed order, as effectively done in the PSM approach. Within the expansion by regions, especially in simple cases with only two relevant regions (here hard and potential), double expansions usually yield the same doubly-expanded integrand, whether the two expansions are executed in one order or the other. So we can expect that the identity $T^{(p)}T^{(h)}I = T^{(h)}T^{(p)}I \equiv T^{(h,p)}I$ holds. Let us consider in the following at first the case without invariant-mass restrictions, so that I does not depend on any cut Λ . Then our second important remark is that the integration of the integrand $T^{(h,p)}I$ over p_t vanishes in dimensional regularization,

$$F^{(h,p)} = \int d^d p_t T^{(h,p)}I = 0, \quad (57)$$

because after doubly expanding the integrand according to hard and potential momenta, there is no scale left in the integrand (recall that we have not imposed any invariant-mass constraints in I , so the integration limits are unbounded). If we now rewrite (57) using $1 = \theta(x - y) + \theta(y - x)$ as

$$0 = \int d^d p_t \theta(\Lambda^2 - (m_t^2 - p_t^2)) T^{(h,p)}I + \int d^d p_t \theta((m_t^2 - p_t^2) - \Lambda^2) T^{(h,p)}I, \quad (58)$$

we readily identify the first term as the Taylor series in (Λ/m_t) of the non-resonant contributions computed in our approach for an invariant-mass cut of the form (12). The second term corresponds to the resonant NRQCD amplitude further expanded assuming hard p_t and integrated outside the region of p_t^2 allowed by the invariant-mass cuts. That is precisely the quantity that yields minus the series in the first term of (56) with powers of Λ , obtained in the phase-space matching approach. Therefore, from (58) we conclude that the PSM contributions must be equal to the series expansion obtained with the unstable-particle EFT, as we have shown by explicit computation up to terms of order $(m_t/\Lambda)^0 \log \Lambda$. The equivalence between both series is lost at the order where terms coming from full-theory diagrams with just one top or antitop, or with no tops at all, which are not described by NRQCD, first contribute. As mentioned before, these terms arise at NLO from diagrams $h_5 - h_{10}$, and are of order $\Gamma_t \Lambda^3/m_t^4$. Since the $\mathcal{O}(\alpha_s)$ corrections to diagrams $h_5 - h_{10}$ do not introduce negative powers of $(1 - t)$, we also expect that the NNLO non-resonant contributions in the phase-space matching series start to differ from ours at order $\alpha_s \Gamma_t \Lambda^3/m_t^4$.

The reasoning above also provides further insight on the regions (of gluon momenta) which contribute to the endpoint-singular NNLO corrections. In scaleless overlap contributions like (57) where the integrand is doubly expanded according to both regions, singularities from domains of hard and potential top momenta p_t cancel each other to

yield zero. Exactly the same cancellation of singularities happens between the contributions of the individual (hard or potential) regions, originating from the respective integration domain where the top momentum approaches the scaling of the opposite region: The ultraviolet singularities (from the hard- p_t limit) present in the integrals of the resonant contribution (which have been expanded for potential p_t) are canceled by the endpoint singularities (from the potential- p_t limit) of the non-resonant contribution (whose integrals have been expanded for hard p_t). This cancellation occurs individually for the different scalings of gluon momenta. It is known that the $1/\epsilon$ finite-width divergences on the resonant side originate purely from potential (Coulomb) gluons. So their cancellation must be provided purely by potential gluon momenta in the endpoint-divergent non-resonant diagrams. This is exactly what we have found in our calculation for the origin of the $1/\epsilon_{\text{ep}}$ terms from potential-region contributions.

Similarly, it is known that ultrasoft gluons do not contribute to the total resonant NRQCD amplitudes at NNLO. So it comes without surprise that we observe a cancellation of the ultrasoft-region contributions to the endpoint-divergent non-resonant corrections (see the remarks at the end of Sec. 4.2).

5.2 Comparison with an approach based on expanding in $\rho = 1 - M_W/m_t$

A different path has been taken by the authors of Ref. [33] to provide an estimate of the NNLO non-resonant corrections. They have expanded the NNLO non-resonant contributions to the $t\bar{t}$ total cross section in powers of $\sqrt{\rho}$, where $\rho = 1 - M_W/m_t \approx 0.5$, and calculated the first two terms in this expansion. For the NLO non-resonant corrections, the leading-order term in ρ has been shown to deviate from our exact result [28] by less than 5%, despite the fact that the approximation for the individual diagrams is much less accurate. Such a numerical comparison is not possible at NNLO where the exact result is not known, and our approximation, Eq. (52), does not correspond to the total cross section, but to the cross section with invariant-mass cuts applied in the bW pairs.

We notice though important differences between the approach followed in [33] and ours for the NNLO result. According to the authors of [33] the leading-order term in ρ of the NNLO non-resonant contributions arises from diagram h_{1a} and contains an energy-dependent term of the form $\log(v/\rho)$. The latter is generated in their approach because the scale m_tv^2 in the top-quark propagators is kept as an infrared regulator for the (infrared-divergent) loop integration of the non-resonant amplitude, despite the fact that the integral is saturated by the region $|\vec{p}| \sim \rho^{1/2}m_t \gg m_tv$. Let us remark that in our approach logarithms of the velocity can only appear in the resonant matrix elements, because the hard-momentum expansion performed in the non-resonant diagrams drops terms of order E , $\Gamma_t \sim m_tv^2$ from the top-quark propagators and, as a consequence, an energy-dependence there only arises beyond NNLO as powers of E . The infrared divergence in [33] is analogous to the $1/\epsilon_{\text{ep}}$ endpoint divergences we find within the unstable-particle EFT formalism, and must be compensated by an ultraviolet divergence arising from a resonant contribution in order to render the leading-order result in the

ρ -expansion independent of the regularization scheme.⁴ The need for an ultraviolet counterpart for the result of [33] becomes even clearer if the infrared divergence on the non-resonant side is regulated dimensionally, which substitutes the $\log v$ above by a $\log \mu$ plus (potentially) additional finite terms, thus introducing an explicit scheme-dependence through the renormalization scale μ . We can easily do this exercise by taking the integral form of the leading-order term provided in Eq. (4.1) of [33] and performing it in d dimensions. With the appropriate normalization factor for the cross section, this contribution reads

$$\delta\sigma_{\text{non-res}}^{(2),\rho^{-1}} = \frac{4\pi\alpha^2}{3s} \left[Q_t^2 Q_e^2 + \frac{2Q_e Q_t v_e v_t}{1 - M_Z^2/(4m_t^2)} + \frac{(a_e^2 + v_e^2)v_t^2}{(1 - M_Z^2/(4m_t^2))^2} \right] \frac{N_c \Gamma_t^{\text{Born}}}{m_t} \delta_{1a}^{(1)} \Big|_{\rho^{-1}}, \quad (59)$$

with

$$\delta_{1a}^{(1)} \Big|_{\rho^{-1}} = 3 \left[\frac{1}{2\epsilon} + \ln \left(\frac{\mu^2}{\rho m_t^2} \right) + 1 \right] \frac{C_F \alpha_s}{\rho}. \quad (60)$$

As expected, the coefficient of the infrared-divergent $1/\epsilon$ term in $\delta\sigma_{\text{non-res}}^{(2),\rho^{-1}}$ above agrees with the $1/\epsilon_{\text{ep}}$ term which arises from our result for diagram h_{1a} , Eq. (32) plus symmetric contributions, expanded at the leading order for small ρ (note that $x = M_W^2/m_t^2 = (1-\rho)^2$ and that the coefficient of $v_t^L v_t^R/\epsilon_{\text{ep}}$ in (32) is proportional to $1/(1-x) \simeq 1/(2\rho)$). A quick inspection of the rest of the $1/\epsilon_{\text{ep}}$ endpoint-divergent results computed in Sec. 4 reveals that diagram h_{1b} also contains an infrared $1/\epsilon_{\text{ep}}$ divergence proportional to ρ^{-1} . It can also be checked that the sum of the $\rho^{-1}/\epsilon_{\text{ep}}$ divergences from diagrams h_{1a} and h_{1b} (including symmetric contributions) cancels against the first term in the ρ -expansion of the finite-width divergence on the resonant side, Eq. (10). The contribution from diagram h_{1b} has not been considered, however, in the analysis of the $1/\rho$ term of [33]. We therefore conclude that in its present form the leading-order NNLO non-resonant result of [33] is incomplete, and cannot be consistently added as a correction to the known NNLO contributions from the resonant side.

Finally, for implementing a loose cut on the bW invariant masses in the integrals for the NLO non-resonant contributions expanded in the parameter ρ , the authors of [33] have provided the replacement rule $\rho m_t^2 \rightarrow \Lambda^2/2$ applied to the arguments of the theta-functions of their integrals. Adopting the same rule for the $\mathcal{O}(\alpha_s)$ contribution that yields the leading non-resonant term at NNLO in the approach of [33], the same m_t^2/Λ^2 term as in our result (52) is obtained. Our subleading terms of order m_t/Λ cannot directly be compared to [33].

⁴The leading-order NNLO non-resonant term in [33] is proportional to $\alpha_s \Gamma_t/\rho$. While the NNLO relativistic corrections to the resonant diagram with a Coulomb potential, Fig. 1, only give terms scaling as $\alpha_s \Gamma_t \times \mathcal{O}(\rho^0)$, the corrections arising from the insertion of the (electroweak) absorptive matching coefficients $C_p^{(v/a),\text{abs}}$ into Fig. 1 yield terms scaling also as $\alpha_s \Gamma_t/\rho$. Part of the latter provides the counterpart for the infrared divergence in the leading-order result from [33].

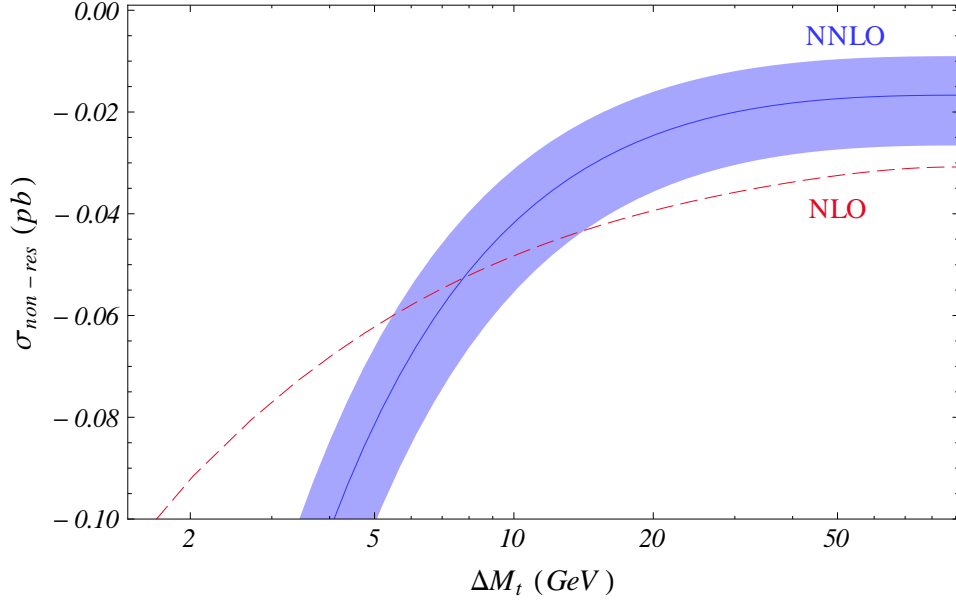


Figure 5: Endpoint-singular NNLO non-resonant contribution to the $t\bar{t}$ cross section computed at $s = 4m_t^2$ as a function of the invariant-mass cut $\Delta M_t = m_t(1 - \sqrt{1 - \Lambda^2/m_t^2})$. The solid (blue) line corresponds to $\sigma_{\text{non-res}}^{(2),\text{ep}}$ in (52) dropping the $1/\epsilon_{\text{ep}}$ term, and using $\alpha_s \equiv \alpha_s(\mu_{\text{soft}})$ with $\mu_{\text{soft}} = 30$ GeV. The shaded (blue) band shows the same result varying μ_{soft} in the interval 15–60 GeV. For comparison, the NLO non-resonant contribution (dashed red line), $\sigma_{\text{non-res}}^{(1)}$ from [28], is also shown.

6 Final results

In this final section we compare numerically the first terms in the (Λ/m_t) -series of the NNLO non-resonant corrections with the NLO ones as well as with the leading-order EFT approximation. This is done for the $e^+e^- \rightarrow W^+W^-b\bar{b}$ cross section with invariant-mass cuts in the bW subsystems of the form (12), where $\Lambda^2 = 2m_t\Delta M_t - \Delta M_t^2$. The NNLO non-resonant terms are given by the endpoint-singular contributions computed in Sec. 4, and have been collected in Eq. (52). The NLO non-resonant corrections, $\sigma_{\text{non-res}}^{(1)}$, are obtained from the results given in [28], which are too lengthy to be reproduced here. We present NLO and NNLO contributions separately in this section, *i.e.* “NNLO” always refers to the pure second-order corrections without including the NLO result.

A dependence on the invariant-mass cut ΔM_t enters first at NLO through the non-resonant contributions for the case of loose cuts (*i.e.* $\Delta M_t \gg \Gamma_t$). The leading-order cross section $\sigma_{t\bar{t}}^{(0)}$ is given entirely by the leading-order resonant contribution (2), which sums Coulomb corrections proportional to $(\alpha_s/v)^n$ to all orders in the strong coupling. Its analytic expression, following the same conventions as in this paper, can be found in [28]. $\sigma_{t\bar{t}}^{(0)}$ depends on the renormalization scale μ_{soft} only through $\alpha_s(\mu_{\text{soft}})$.

Figure 5 shows the contribution to the cross section from the NNLO endpoint-singular terms as a function of the invariant-mass cutoff exactly at the threshold ($s = 4m_t^2$). The NNLO contribution corresponds to $\sigma_{\text{non-res}}^{(2),\text{ep}}$ in (52) with the endpoint divergence $1/\epsilon_{\text{ep}}$ removed. It uses $\alpha_s \equiv \alpha_s(\mu_{\text{soft}})$ plus the Standard-Model input parameters

$$M_Z = 91.1876 \text{ GeV} , \quad M_W = 80.398 \text{ GeV} , \quad m_t = 172.0 \text{ GeV} ,$$

$$G_\mu = 1.166367 \times 10^{-5} \text{ GeV}^{-2} , \quad V_{tb} = 1 , \quad (61)$$

whereas the on-shell Weinberg angle $c_w = M_W/M_Z$ and the fine-structure constant in the G_μ -scheme, $\alpha \equiv \sqrt{2}G_\mu M_W^2 s_w^2/\pi$, are derived quantities. The solid (blue) line is obtained for $\mu_{\text{soft}} = 30 \text{ GeV}$, where $\alpha_s(30 \text{ GeV}) = 0.142$, whereas the shaded band displays the effect of varying the scale μ_{soft} from 15 to 60 GeV (lower values of the scale corresponding to more negative contributions). The dashed (red) line is the NLO non-resonant contribution $\sigma_{\text{non-res}}^{(1)}$ from [28] which is also shown for comparison. Both the NLO and NNLO non-resonant corrections give a negative shift.

The values shown in Fig. 5 range from $\Delta M_t = \Gamma_t \simeq 1.46 \text{ GeV}$ up to the maximum value allowed by the kinematics, $\Delta M_{t,\text{max}} = m_t - M_W \simeq 91.6 \text{ GeV}$, which corresponds to the total cross section. Recall that the NNLO non-resonant terms computed in this work are a valid description for moderate invariant-mass cuts, satisfying $\Gamma_t \ll \Delta M_t \ll m_t$. For tight cuts ($\Delta M_t \lesssim \Gamma_t$), which are not studied here, the expansion by regions dictates that the dependence on ΔM_t is taken into account in the resonant part of the amplitude, while the non-resonant contributions are absent in this case (see [28]). The further requirement $\Delta M_t \ll m_t$ is a consequence of the expansion around the endpoint that produces the result (52) for the non-resonant contributions. From Fig. 5 we observe that in a moderate ΔM_t -range ($\Delta M_t \gtrsim 6\Gamma_t \approx 9 \text{ GeV}$) the NNLO non-resonant corrections are always smaller (in absolute value) than the NLO ones, and (because of the higher singularity in Λ or ΔM_t) they become more negative when the available phase space for the bW pairs gets restricted by tightening the invariant-mass cut. The ratio between the NNLO and NLO non-resonant contributions ranges approximately from 0.9 to 0.5 for ΔM_t in the interval (10, 40) GeV.

The relative size of the endpoint-singular NNLO corrections with respect to the LO cross section as a function of the centre-of-mass energy in the threshold region is displayed in Figure 6 for two different values of the invariant-mass cut, $\Delta M_t = 35 \text{ GeV}$ (upper blue solid line) and $\Delta M_t = 15 \text{ GeV}$ (upper blue dashed line). The corresponding curves for the NLO result are also shown (lower black lines). At threshold energies, $|\sqrt{s} - 2m_t| \ll 2m_t$, the non-resonant corrections are almost energy-independent, with a mild linear energy-dependence introduced from the Z and photon propagators. The NNLO non-resonant corrections for the chosen values of ΔM_t give a constant negative shift of about 2 – 3% above the threshold where the LO cross section is also constant. Below the peak region, where the LO result vanishes rapidly, the relative size of the non-resonant corrections is very large, up to 10% for $\Delta M_t = 35 \text{ GeV}$ in the energy range shown in Fig. 6. In absolute value, the endpoint-singular NNLO non-resonant

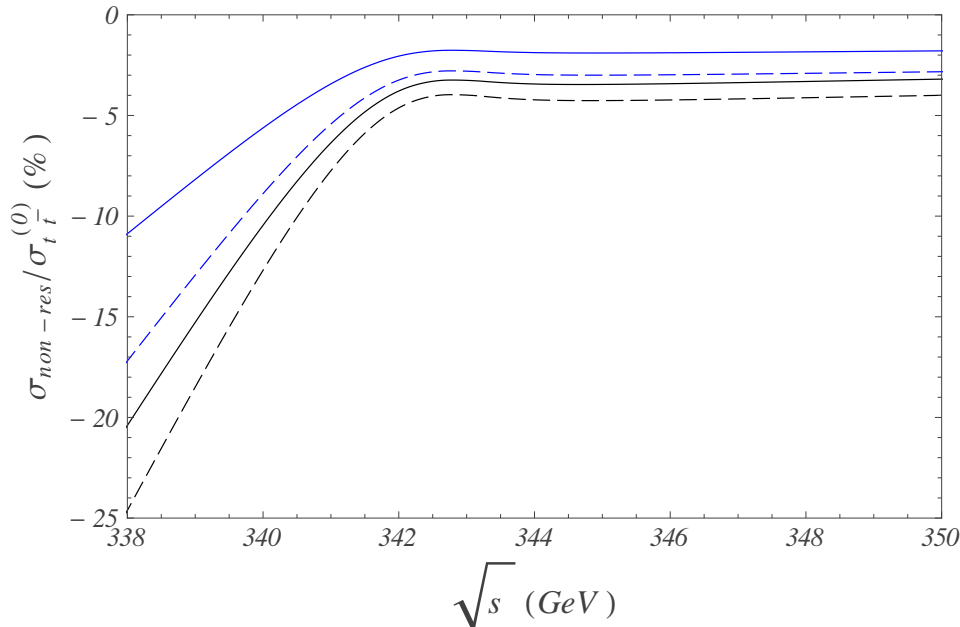


Figure 6: Relative sizes of the non-resonant corrections with respect to the $t\bar{t}$ LO cross section in percent: $\sigma_{\text{non-res}}^{(2),\text{ep}}/\sigma_{t\bar{t}}^{(0)}$ (upper blue lines) and $\sigma_{\text{non-res}}^{(1)}/\sigma_{t\bar{t}}^{(0)}$ (lower black lines, from [28]). Solid (dashed) lines correspond to an invariant-mass cut $\Delta M_t = 35$ GeV ($\Delta M_t = 15$ GeV). The renormalization scale in the NNLO non-resonant contribution has been set to $\mu_{\text{soft}} = 30$ GeV, and we have chosen $\alpha_s(30 \text{ GeV}) = 0.142$ for the value of the QCD coupling that enters also in the LO result.

corrections amount to 32–28 fb for $\Delta M_t = 15$ GeV and 20–18 fb for $\Delta M_t = 35$ GeV when the centre-of-mass energy is varied within the interval (338, 350) GeV.

For an analysis of the impact of higher-order non-resonant corrections for moderate invariant-mass cuts not considered in the present work, namely the non-logarithmic terms of order $(\Lambda/m_t)^0$ and a large part of the N³LO contributions, we refer the reader to [30].

7 Summary

The corrections induced by off-shell top-quark decay and by other non-resonant production processes of the physical $W^+W^-b\bar{b}$ final state are a missing piece towards the prediction of the threshold top-quark pair production cross section at the third order (NNLO). Phenomenologically, they are needed to match the accuracy of the well-known QCD corrections to the resonant production, as required for the precision attainable in the top-mass determination at a future e^+e^- collider. The computation of the full set of NNLO non-resonant corrections represents a non-trivial task, involving $\mathcal{O}(100)$ diagrams that include 1-loop virtual-QCD as well as tree-level gluon-radiation corrections to the bWt final state.

At the theory level, the NNLO non-resonant corrections are also mandatory, because the purely resonant cross section contains at the same order an uncanceled ultraviolet divergence, $\text{div } \sigma_{\text{res}}^{\text{NNLO}} \propto \alpha_s \Gamma_t / \epsilon$ (10), which must be compensated by a divergence with opposite sign on the non-resonant side in order to yield a regularization-independent result for this observable. In this work we have identified the divergences in the NNLO non-resonant amplitudes which provide such a cancellation. They originate at the endpoint of the phase-space integration over the bW invariant mass in virtual diagrams with bWt final states. We have extracted these endpoint divergences through an expansion of the relevant NNLO non-resonant diagrams around the endpoint. The expanded integrals involve the scale Λ^2 of the invariant-mass cut in the bW system. In this way, apart from the $1/\epsilon$ divergences, we obtain the endpoint-singular terms $(m_t/\Lambda)^2$, (m_t/Λ) and $(m_t/\Lambda)^0 \log \Lambda$ which correspond to the first terms in the expansion in powers of (Λ/m_t) . This series provides a rigorous approximation of the NNLO non-resonant contributions to the $e^+e^- \rightarrow W^+W^-b\bar{b}$ cross section with symmetric invariant-mass cuts of size $\Lambda^2 \approx 2m_t\Delta M_t$ applied to the bW pairs, as long as ΔM_t is much smaller than the top mass but significantly larger than the top width (equivalently, if $m_t\Gamma_t \ll \Lambda^2 \ll m_t^2$).

Our analytic result agrees with the one obtained for the same observable within the phase-space matching approach [30]. On the other hand, by comparing the infrared structure of our result with the one obtained in [33] at leading order in the expansion for small $\rho = 1 - M_W/m_t$, we conclude that the latter misses one contribution and that it cannot be combined with the NNLO resonant corrections in a regularization-scheme independent way. Numerically we find that within the above range of invariant-mass cuts the NNLO non-resonant contributions produce a negative shift of about 2 – 3% with respect to the leading-order $t\bar{t}$ cross section above threshold. For energies below the peak, where non-resonant production is known to dominate over the (subleading) resonant terms, the corrections reach up to 10 – 15%.

The presence of endpoint singularities in the NNLO non-resonant contributions represents an additional complication for their calculation, since these singularities have to be subtracted from the amplitude, together with the standard soft-collinear divergences due to gluon radiation. The analysis performed in this work, which identifies and evaluates the endpoint-singular terms, thus provides a necessary step towards the computation of the full set of NNLO non-resonant contributions to $e^+e^- \rightarrow W^+W^-b\bar{b}$ and, consequently, towards having a complete NNLO theoretical prediction for $t\bar{t}$ production near threshold that accounts for the effects related to top-quark decay in a consistent manner.

Acknowledgments

We thank M. Beneke for helpful discussions and for his comments on the manuscript. We also thank A. A. Penin for discussions on the comparison with their result. This work is supported by the DFG Sonderforschungsbereich/Transregio 9 “Computergestützte Theoretische Teilchenphysik”. The work of P. R. is partially supported by MEC (Spain) under grants FPA2007-60323 and FPA2011-23778 and by the Spanish Consolider-Ingenio 2010 Programme CPAN (CSD2007-00042). Feynman diagrams have been drawn with the

packages AXODRAW [39] and JAXODRAW [40]. We acknowledge the use of the computer programs FORM [41] and FEYNCALC [42] for some parts of the calculation.

References

- [1] M. Martinez and R. Miquel, Eur. Phys. J. C **27** (2003) 49, hep-ph/0207315.
- [2] K. Seidel, F. Simon, M. Tesar and S. Poss, Eur. Phys. J. C **73** (2013) 2530, arXiv:1303.3758 [hep-ex].
- [3] T. Aaltonen *et al.* [CDF and D0 Collaborations], Phys. Rev. D **86** (2012) 092003, arXiv:1207.1069 [hep-ex].
- [4] ATLAS Collaboration, ATLAS-CONF-2012-095.
- [5] I. I. Y. Bigi, Y. L. Dokshitzer, V. A. Khoze, J. H. Kühn and P. M. Zerwas, Phys. Lett. B **181** (1986) 157.
- [6] V. S. Fadin and V. A. Khoze, JETP Lett. **46** (1987) 525.
- [7] V. S. Fadin and V. A. Khoze, Sov. J. Nucl. Phys. **48** (1988) 309.
- [8] M. J. Strassler and M. E. Peskin, Phys. Rev. D **43** (1991) 1500.
- [9] W. E. Caswell and G. P. Lepage, Phys. Lett. B **167** (1986) 437.
- [10] A. H. Hoang *et al.*, Eur. Phys. J. direct C **2** (2000) 1, hep-ph/0001286.
- [11] M. Beneke, Y. Kiyo and K. Schuller, Nucl. Phys. B **714** (2005) 67, hep-ph/0501289.
- [12] M. Beneke, Y. Kiyo and K. Schuller, PoS (RADCOR 2007) 051, arXiv:0801.3464 [hep-ph].
- [13] M. Beneke and Y. Kiyo, Phys. Lett. B **668** (2008) 143, arXiv:0804.4004 [hep-ph].
- [14] A. Pineda and J. Soto, Nucl. Phys. Proc. Suppl. **64** (1998) 428, hep-ph/9707481.
- [15] M. Beneke, hep-ph/9806429.
- [16] M. Beneke, A. Signer and V. A. Smirnov, Phys. Lett. B **454** (1999) 137, hep-ph/9903260.
- [17] N. Brambilla, A. Pineda, J. Soto and A. Vairo, Nucl. Phys. B **566** (2000) 275, hep-ph/9907240.
- [18] M. E. Luke, A. V. Manohar and I. Z. Rothstein, Phys. Rev. D **61** (2000) 074025, hep-ph/9910209.

- [19] A. V. Manohar and I. W. Stewart, Phys. Rev. D **62** (2000) 014033, hep-ph/9912226.
- [20] A. H. Hoang and I. W. Stewart, Phys. Rev. D **67** (2003) 114020, hep-ph/0209340.
- [21] A. H. Hoang, A. V. Manohar, I. W. Stewart and T. Teubner, Phys. Rev. Lett. **86** (2001) 1951, hep-ph/0011254.
- [22] A. H. Hoang, A. V. Manohar, I. W. Stewart and T. Teubner, Phys. Rev. D **65** (2001) 014014, hep-ph/0107144.
- [23] A. Pineda and A. Signer, Nucl. Phys. B **762** (2007) 67, hep-ph/0607239.
- [24] M. Stahlhofen and A. Hoang, PoS (RADCOR 2011) 025, arXiv:1111.4486 [hep-ph].
- [25] M. Beneke, A. P. Chapovsky, A. Signer and G. Zanderighi, Phys. Rev. Lett. **93** (2004) 011602, hep-ph/0312331.
- [26] M. Beneke, A. P. Chapovsky, A. Signer and G. Zanderighi, Nucl. Phys. B **686** (2004) 205, hep-ph/0401002.
- [27] M. Beneke, P. Falgari, C. Schwinn, A. Signer and G. Zanderighi, Nucl. Phys. B **792** (2008) 89, arXiv:0707.0773 [hep-ph].
- [28] M. Beneke, B. Jantzen and P. Ruiz-Femenía, Nucl. Phys. B **840** (2010) 186, arXiv:1004.2188 [hep-ph].
- [29] A. H. Hoang, C. J. Rei er and P. Ruiz-Femenía, Nucl. Phys. Proc. Suppl. **186** (2009) 403, arXiv:0810.2934 [hep-ph].
- [30] A. H. Hoang, C. J. Rei er and P. Ruiz-Femenía, Phys. Rev. D **82** (2010) 014005, arXiv:1002.3223 [hep-ph].
- [31] A. H. Hoang and C. J. Rei er, Phys. Rev. D **71** (2005) 074022, hep-ph/0412258.
- [32] P. Ruiz-Femenía, arXiv:1203.0934 [hep-ph].
- [33] A. A. Penin and J. H. Piclum, JHEP **1201** (2012) 034, arXiv:1110.1970 [hep-ph].
- [34] M. Beneke and V. A. Smirnov, Nucl. Phys. B **522** (1998) 321, hep-ph/9711391.
- [35] V. A. Smirnov, *Applied asymptotic expansions in momenta and masses*, vol. 177 of *Springer Tracts in Modern Physics*, Springer, Germany (2002).
- [36] B. Jantzen, JHEP **1112** (2011) 076, arXiv:1111.2589 [hep-ph].
- [37] M. Jezabek and J. H. K hn, Nucl. Phys. B **314** (1989) 1.
- [38] S. Actis, M. Beneke, P. Falgari and C. Schwinn, Nucl. Phys. B **807** (2009) 1, arXiv:0807.0102 [hep-ph].

- [39] J. A. M. Vermaseren, Comput. Phys. Commun. **83** (1994) 45.
- [40] D. Binosi, J. Collins, C. Kaufhold and L. Theussl, Comput. Phys. Commun. **180** (2009) 1709, arXiv:0811.4113 [hep-ph].
- [41] J. A. M. Vermaseren, math-ph/0010025.
- [42] R. Mertig, M. Böhm and A. Denner, Comput. Phys. Commun. **64** (1991) 345.